

Triple-cation perovskite solar cells fabricated by hybrid PVD/blade coating process using green solvents

*Severin Siegrist, Shih-Chi Yang, Evgeniia Gilshtein, Xiaoxiao Sun, Ayodhya N. Tiwari and Fan Fu**

Laboratory for Thin Films and Photovoltaics, Empa – Swiss Federal Laboratories for Materials Science and Technology, Ueberlandstrasse 129, 8600 Duebendorf, Switzerland

*Email: fan.fu@empa.ch

ABSTRACT

The scalability of highly efficient organic-inorganic perovskite solar cells (PSCs) is one of the remaining challenges of solar module manufacturing. Various scalable methods have been explored to strive for uniform perovskite films of high crystal quality on large-area substrates. However, each of these methods have individual drawbacks, limiting the successful commercialization of perovskite photovoltaics. Here, we report a fully scalable hybrid process, which combines vapor- and solution-based techniques to deposit high quality uniform perovskite films on large-area substrates. This two-step process does not use toxic solvents, and it further allows facile implementation of passivation strategies and additives. We fabricated PSCs based on this process and used blade coating to deposit both charge transporting layers (SnO_2 and Spiro-OMeTAD) without hazardous solvents in ambient air. The fabricated PSCs have yielded open-circuit voltage up to 1.16 V and power conversion efficiency of 18.7 % with good uniformity on 5 cm x 5 cm substrates.

Introduction

Organic–inorganic halide perovskite solar cells (PSC) have shown tremendous advancements in the past ten years, now reaching certified power conversion efficiency (PCE) of 25.5 %¹. This rapid development can be mainly attributed to the excellent optoelectronic properties of the perovskite material and to the development of facile perovskite fabrication^{2, 3, 4, 5, 6, 7}. One of the remaining challenges towards successful commercialization of perovskite photovoltaics is to fabricate every layer of the PSC by scalable deposition methods and to demonstrate high performance devices on large-area. Generally, these scalable deposition methods can be divided into solution- and vapor-based techniques. Solution-based methods, such as blade coating^{8, 9}, slot-die coating^{10, 11}, inkjet printing^{1, 12}, spray coating¹³ offer the possibility to mix additives into the precursor solution for controlling the film formation^{14, 15} as well as to implement passivation strategies for improving efficiency and stability¹⁶. Among the solution-based methods, blade coating is a promising, scalable technique due to its excellent material usage rate (~ 95 %) and high throughput capabilities¹⁷. Over the past few years, Huang's group has developed various strategies to improve the film uniformity over large areas as well as the device performance by compositional engineering¹⁸ as well as by mixing surfactants¹⁵, dopants¹⁹, additives¹⁶, and solvents²⁰. Recently, they discovered a substantial void fraction in the buried perovskite/hole transporting layer interface induced by trapped dimethyl sulfoxide (DMSO) during film formation. The interfacial void fraction was reduced by partially substituting DMSO with solid-state carbonylhydrazide to achieve 23.6 % efficient p-i-n PSC and 19.2 % efficient mini-module with an aperture area of 50 cm² by blade coating²¹. However, to dissolve the inorganic halide precursors, solvents like 2-methoxyethanol (2-ME) or alternatively, N,N-dimethylformamide (DMF) are usually used^{22, 20}, which have been known for their reproductive toxicity (Category 1B, H360),

bearing risk to workers and environment^{23, 24, 25}. Moreover, it is challenging to form conformal films on rough surfaces, needed for monolithically integrated perovskite/silicon or perovskite/CIGS tandem solar cells^{26, 27}. These drawbacks could be overcome by using vapor-based techniques^{28, 29, 30}. For example, Li et al. co-evaporated methylammonium iodide (MAI) and lead iodide (PbI₂) to obtain PSCs with PCE of 20.28 % for 0.16 cm² small-area device and 18.13 % for 21 cm² perovskite mini-module³¹. Liu et al. sequentially evaporated PbI₂, formamidinium iodide (FAI) and cesium iodide (CsI) to fabricate uniform small-area devices (0.09 cm²) on large-area substrate (400 cm²)³². Although, the uniformity of vapor-based techniques is impressive, it is very challenging to implement passivation strategies or controlling the perovskite composition that is essential for high performance and superior stability³³.

In this work, we report a novel and scalable fabrication process of the perovskite film that combines the merits of the scalable solution- and vapor-based deposition methods, including facile compositional engineering to broadly tune the bandgap, and more importantly the avoidance of using toxic solvents. This hybrid PVD/blade coating process involves three steps – physical vapor deposition, blade coating and thermal annealing. We systematically vary the processing conditions of the perovskite absorber to gain insights into the perovskite formation mechanism during this process. We fabricated PSC devices with blade coated charge transporting layers (SnO₂ and Spiro-OMeTAD) in ambient air with green solvents. These devices achieved high open-circuit voltage (V_{OC}) up to 1.16 V for a perovskite with an optical bandgap of 1.56 eV and a PCE up to 18.7 %, which is the highest reported efficiency of scalable and solution-based PSCs using green solvents only.

Hybrid PVD/blade coating fabrication process for scalable perovskite films

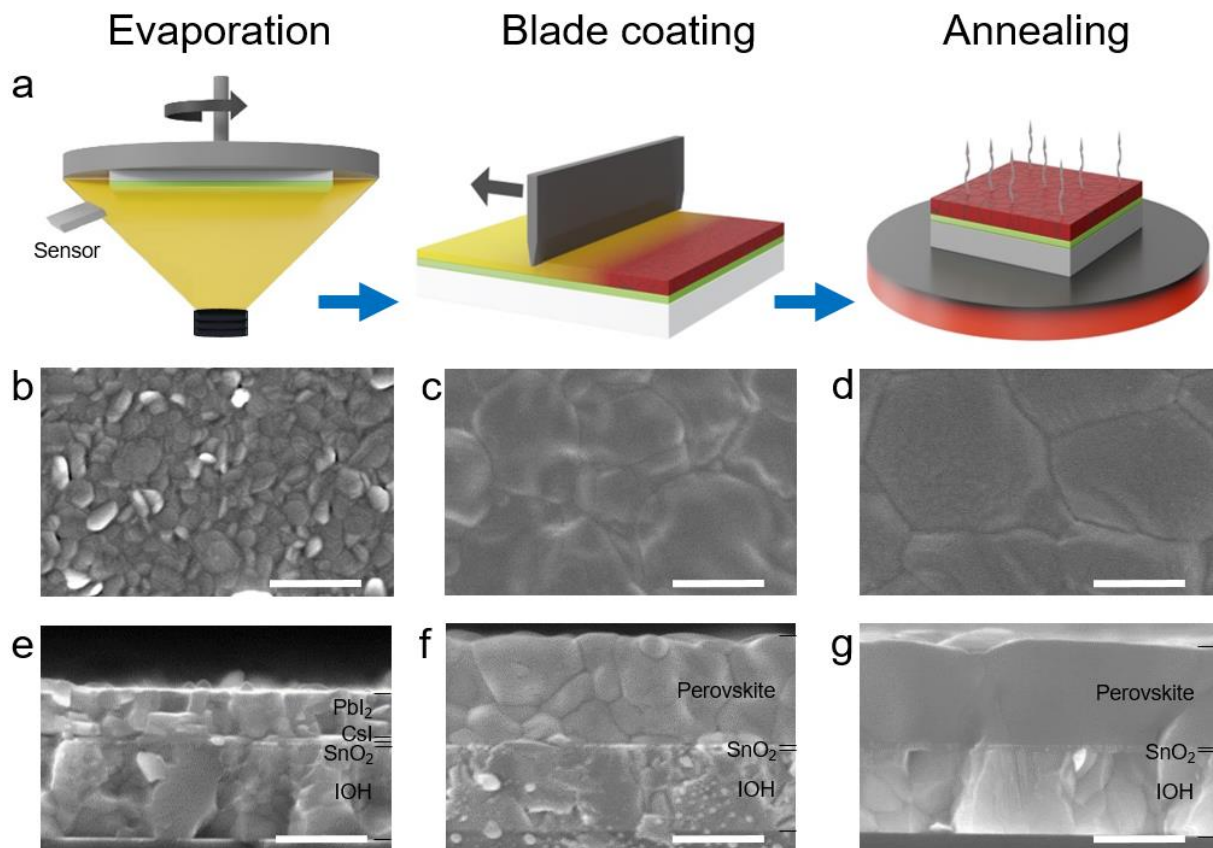


Figure 1: Hybrid PVD/blade coating process for perovskite absorber layer and morphology after each step. a) Schematic of the three-step PVD/blade coating fabrication process. SEM top and cross-section view images after each fabrication step: b, e) after evaporation, c, f) after blade coating and d, g) after thermal annealing. The scale bar is 500 nm.

Figure 1a shows the schematic of the scalable PVD/blade coating process to fabricate the perovskite layer. This hybrid process is composed of three steps. In the first step, the inorganic halide template is sequentially deposited by thermal evaporation. This template consists of 300 nm lead iodide (PbI_2) on top of 15 nm cesium iodide (CsI) layer. In the second step, the organic halide precursor solution, composed of formamidinium iodide (FAI), methylammonium bromide (MABr), and methylammonium chloride (MACl) dissolved in isopropanol, is blade coated on the

inorganic halide template at substrate temperature of 65 °C. In the last step, thermal annealing at 150 °C for 15 min is performed in ambient air to obtain a compact perovskite film with large crystal grains. To study the film formation and composition, we used blade coated tin oxide (SnO₂) as underlying electron transporting layer and for PSC devices, we used IO:H/SnO₂/perovskite/Spiro-OMeTAD/Au. All deposition by blade coating are done in ambient air and with green solvents only.

Morphology and crystallinity of the perovskite film

In **Figure 1b-g**, scanning electron microscopy (SEM) images depict the film morphology after each step of the PVD/blade coating process. As shown in **Figure 1b**, the PbI₂ layer is composed of elliptical plate-shaped grains. **Figure 1e** shows a smooth and uniform inorganic halide template, which is beneficial for pinhole-free perovskite films³⁴. After blade coating the organic halide solution, most of the inorganic halides are converted into α -phase perovskite even before thermal annealing, evidenced by the XRD pattern in **Figure S1**. This as-deposited perovskite film shows small perovskite grains without voids (**Figure 1c, 1f**) and its thickness is approximately twice the thickness of the inorganic halide template³⁵. Subsequent thermal annealing results in large crystal grains and reduced grain boundaries (**Figure 1d**)³⁶ with comparable surface roughness (**Figure 1g**). We quantified the surface roughness of the film on 5 × 5 μm² area with atomic force microscopy (AFM) to be 8.76 nm after evaporation, 30.2 nm after blade coating, and 34.7 nm after thermal annealing (**Figure S2**).

Perovskite film formation mechanism

In this work, we focus on the processing conditions of the second step - blade coating. For a fixed gap of to 100 μm between blade and substrate, we systematically investigate the organic halide concentration, blade coating speed and substrate temperature to elucidate the influence of

these parameters on the perovskite formation mechanism. First, we use organic halide solutions of different concentration ranging from 10/1/1 to 90/9/9 mg/mL of FAI/MABr/MACl, while maintaining the substrate temperature at 65 °C and the speed at 30 mm/s. The results are shown in **Figure 2** and **Figure S3**.

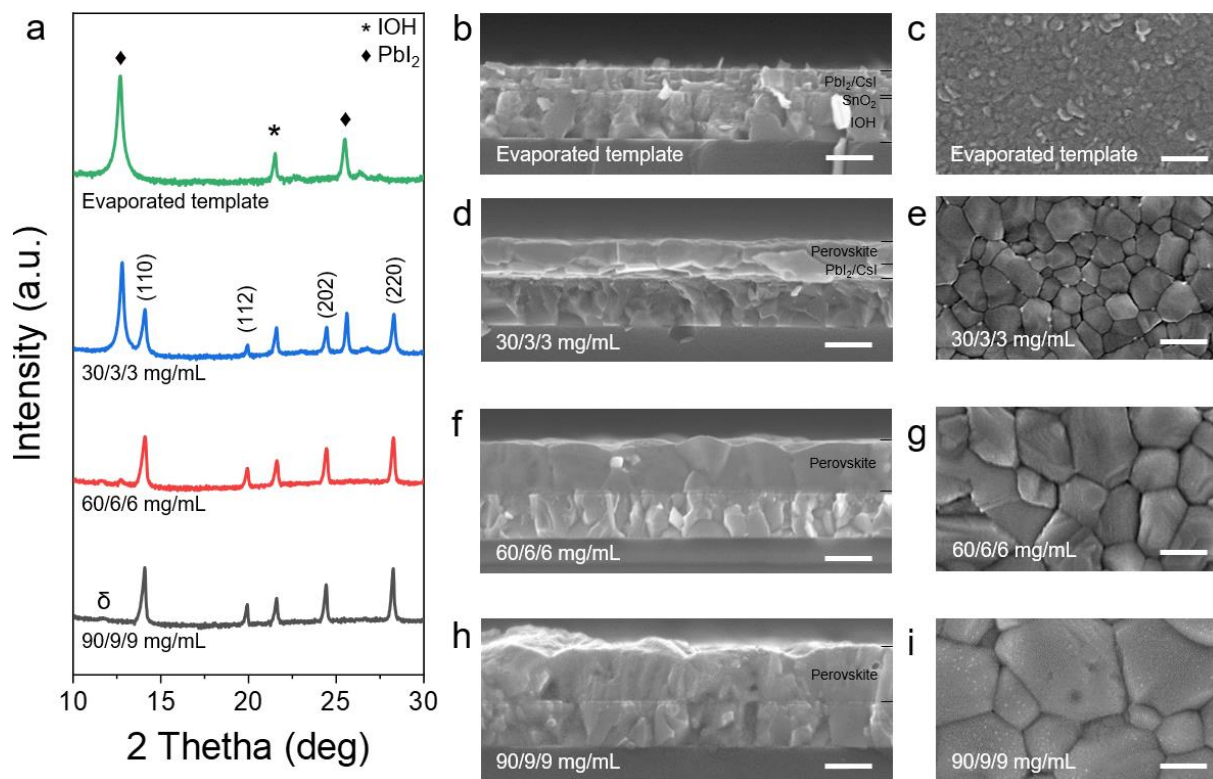


Figure 2: Evaporated inorganic halide template and perovskite films prepared by different concentrations of the organic halide solution. a) XRD patterns (log-scale) with indicated diffraction peaks of the α -phase perovskite crystal planes. PbI_2 is labeled by \blacklozenge and IOH by $*$. b-i) SEM cross-section and top view images of b-c) inorganic halide template and perovskite films prepared by different concentrations: d-e) 30/3/3 mg/mL, f-g) 60/6/6 mg/mL and h-i) 90/9/9 mg/mL of FAI/MABr/MACl. The scale bar is 500 nm.

For low concentrations, 10/1/1 mg/mL (**Figure S3a**) and 30/3/3 mg/mL (**Figure 2a, S3a**), the films have partially converted to perovskite. While the film obtained by 10/1/1 mg/mL appears

yellowish, the film by 30/3/3 mg/mL is brownish, indicating a higher degree of perovskite conversion (**Figure S3b, S3c**). For both concentrations, perovskite has formed in the upper region of the film, whereas residual PbI_2 is located in the lower region. We further detect bright dots at the grain boundaries (**Figure 2e**), which we related to PbI_2 . When we use concentrations between 50/5/5 mg/mL and 70/7/7 mg/mL, the film has converted to perovskite, appearing dark brown (**Figure S3d – f**). While XRD and SEM still show a large amount of unreacted PbI_2 for 50/5/5 mg/mL, for 60/6/6 mg/mL, PbI_2 is almost fully converted to a compact perovskite layer (**Figure 2f, 2g, S3e**). However, using 70/7/7 mg/mL, voids have formed in the perovskite (**Figure S3f**). We suggest that during the coalescence of perovskite grains, no PbI_2 is trapped between adjacent perovskite grains, which could react with the organic halide precursors to prevent the formation of voids (**Figure S4**). Further increasing the concentration to 90/9/9 mg/mL results in defective films with large crystal grains and voids as well as crystallized organic halides, visible as gray dots on the crystal grain surfaces (**Figure 2h, 2i, S3g**). Furthermore, hexagonal perovskite δ -phase³⁷ has formed ($2\theta \approx 11.8^\circ$), making this perovskite film inappropriate for PSC devices (**Figure 2a**).

Next, we use different speeds from 1 mm/s to 90 mm/s and blade coated the organic halide solution with concentration of 60/6/6 mg/mL FAI/MABr/MACl at 65 °C substrate temperature (**Figure S5**). For blade coating, two coating regimes exist, the evaporation regime and the Landau-Levich regime¹⁵. In the evaporation regime (speed ≤ 10 mm/s), slower coating speed yields in thicker layers, i.e. a higher amount of organic halide precursors is supplied due to the increased residence time per unit length. Therefore, the diffraction peak of PbI_2 decreases with reduced speed (1 mm/s) and the perovskite peak intensity increases compared to 10 mm/s (**Figure S5a**). The higher perovskite conversion degree can also be observed by the lower transparency of the sample pictures (**Figure S5b, S5c**), showing incomplete perovskite conversion in the evaporation regime.

With coating speeds > 10 mm/s, the Landau-Levich regime is reached, where viscous forces become dominant, dragging more solution on the substrate with increasing speed³⁸. Hence, the degree of perovskite conversion increases with increasing speed. Using a speed of 30 mm/s, a compact perovskite film with remnant PbI_2 is obtained (**Figure S5d**). The sample shows a uniform coating. With a coating speed ≥ 50 mm/s, no remnant PbI_2 can be detected and the film uniformity is lost. At 50 mm/s, we observe the formation of voids in the perovskite bulk (**Figure S5e**) and the formation of δ -phase perovskite (**Figure S5a**). Interestingly, this δ -phase perovskite has been formed immediately after blade coating at 65 °C. Further increasing the speed, results in large and coarse crystal grains with high crystallinity (**Figure S5f, S5g**).

Lastly, we investigate the influence of different substrate temperatures on the perovskite formation (**Figure S6**), ranging from 25 °C to 75 °. We maintain the coating speed at 30 mm/s and used an organic halide concentration of 60/6/6 mg/mL. For low substrate temperatures ≤ 40 °C, complete perovskite conversion is obtained, enabled by the slower drying rate. However, the complete conversion comes at expense of uniformity due to the coffee-ring effect, which also leads to regions of δ -phase perovskite (**Figure S6b, S6c**). With 55 °C substrate temperature or higher, the coffee-ring effect is suppressed, resulting in uniform coatings. A substrate temperature of 65 °C shows the highest degree of perovskite while maintaining uniformity and crystallinity (**Figure S6e**). At 75 °C, we observe decreasing perovskite conversion as the drying rate is too high, interrupting the perovskite conversion on the surface and leading to remnant PbI_2 on the surface (**Figure S6f**).

To sum up our findings, we show the perovskite film blade coated with 70 mm/s at 65 °C with an organic halide concentration of 60/6/6 mg/ in **Figure S7**. We identify three regions: δ -phase perovskite (**Figure S7d, red**), transition (**Figure S7e, orange**) and α -phase perovskite (**Figure**

S7f, green) and provide the morphologies. We have shown that the organic halide precursor concentration, the coating speed and the substrate temperature play important roles in obtaining uniform perovskite films by the PVD/blade process. Next, we perform depth profiling using time-of-flight secondary ion mass spectroscopy (ToF-SIMS) and X-ray photoelectron spectroscopy (XPS) to shed light on the film composition and the cationic interdiffusion process.

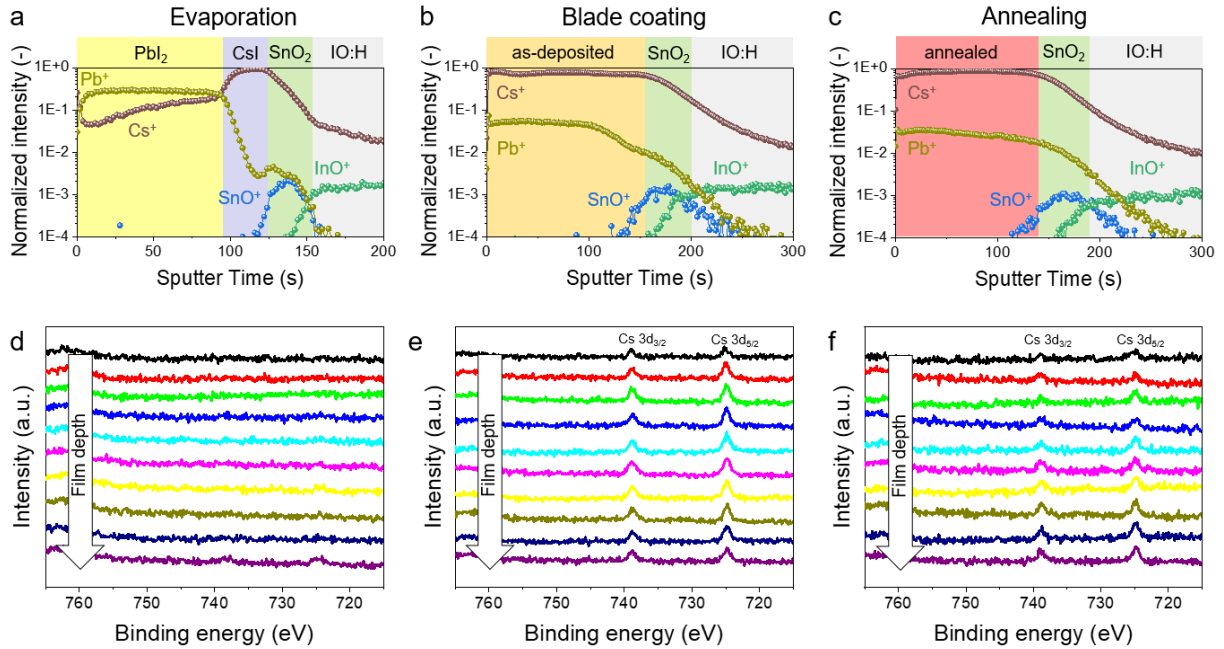


Figure 3: ToF-SIMS depth profiles of (a-c) cation species and depth profiles of XPS Cs 3d spectra at each stage of the hybrid PVD/blade coating process (d-f). The ten lines correspond to profiles at 0 nm, 10 nm, 20 nm, 30 nm, 40 nm, 80 nm, 120 nm, 160 nm, 200 nm and 300 nm depth.

Figure 3 shows the depth profiles obtained by ToF-SIMS and XPS after each step of the PVD/blade coating process. After thermal evaporation, the bilayer of the inorganic template can be clearly differentiated (**Figure 3a**) and Cs 3d peaks in the XPS spectrum can be detected at a profile depth of 300 nm (**Figure 3d**). After blade coating, a uniform signal of Cs cations shows

that Cs species have already diffused (**Figure 3b, S8**) and confirmed by XPS spectrum (**Figure 3e**). After thermal annealing, ToF-SIMS and XPS results are comparable as after blade coating.

Optoelectronic properties of the perovskite film

To evaluate the optoelectronic properties of the perovskite film by PVD/blade coating process, we use two-step spin coated perovskite film (Spin + Spin) as comparison. We show in **Note S1**, that the morphology of the evaporated inorganic halide template remains unchanged when using different amorphous substrates ³⁹. **Figure S9a** compares the absorbance and the photoluminescence (PL) spectra of the perovskite film for both fabrication methods. Both films have the PL peaks at 794 nm (1.56 eV). In **Figure S10**, we provide Tauc plots of these perovskite films and estimated the optical bandgap to be 1.56 eV for both absorbers ⁴⁰. We further investigate the charge recombination dynamics by time-resolved photoluminescence (TRPL) decay measurements (**Figure S9b**). With a bi-exponential fit, we extract the fast decay lifetime τ_1 and the slow decay lifetime τ_2 ⁴¹. The fitting parameters are provided in **Table S1**. The charge carrier lifetimes are comparably long for both perovskite films by PVD/blade (343 ns for τ_1 and 1406 ns for τ_2) and Spin + Spin (396 ns and 1148 ns), showing that perovskite films fabricated by PVD/blade achieve comparable crystal quality and photovoltaic performance (**Figure S11**).

Photovoltaic performance of PSCs by PVD/blade

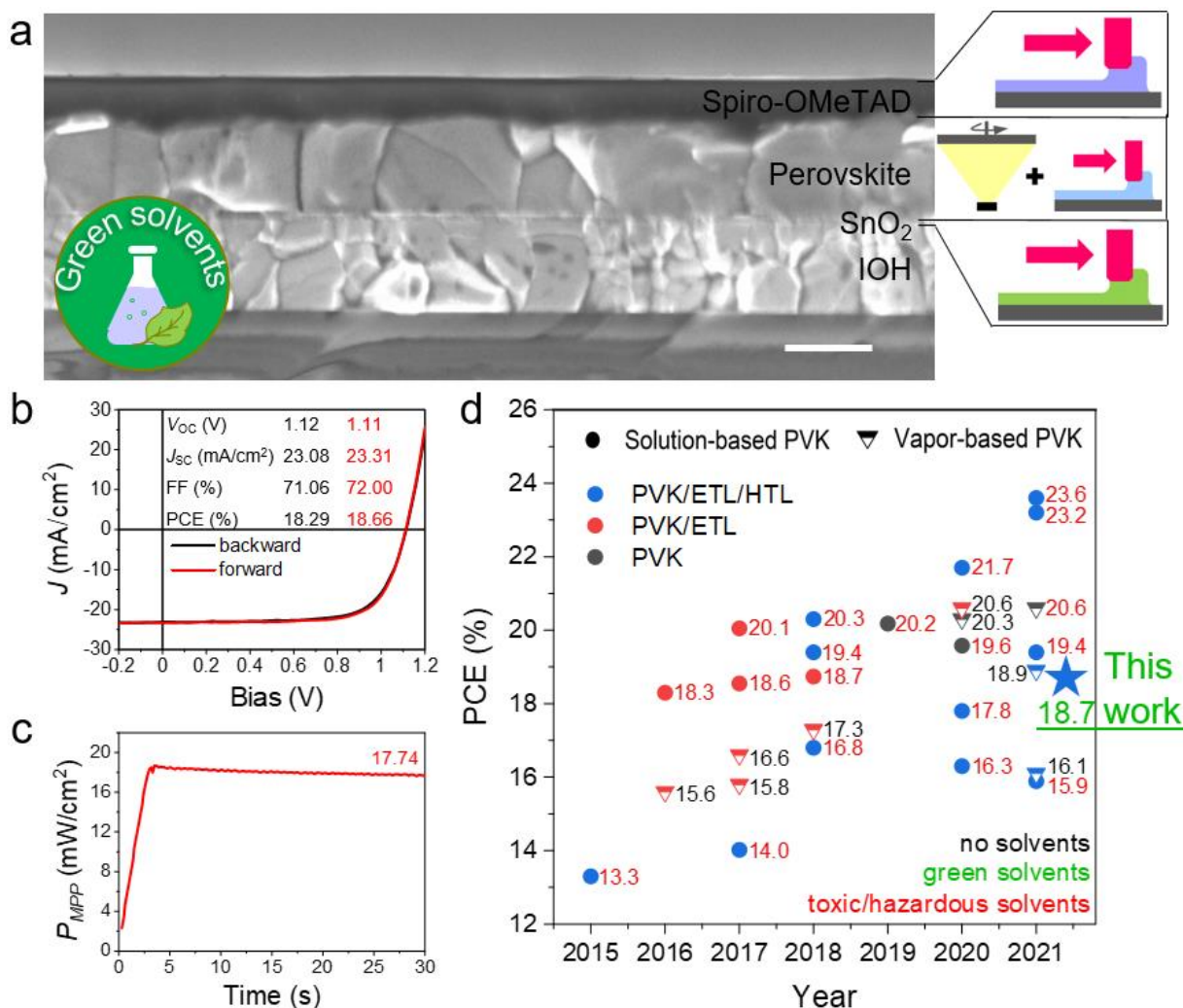


Figure 4: a) SEM cross-section view of PSC with blade coated charge transporting layers and perovskite layer by PVD/blade coating. The scale bar is 500 nm. b) Current-voltage behavior and c) MPP tracking of the champion device. d) Power conversion efficiency versus year for selected, small-area (< 0.1 cm²) devices with indicated layers fabricated by scalable deposition methods (symbol color). Additionally, devices are distinguished by solution- and vapor-based perovskite absorber layer (symbol type) as well as by the use of green or toxic/hazardous in the perovskite fabrication (font color). Perovskite (PVK), electron transporting layer (ETL) and hole transporting layer (HTL).

In **Figure 4**, we evaluate the photovoltaic performance of PSCs with perovskite absorber by PVD/blade process. The n-i-p PSC devices are fabricated on 5 cm x 5 cm substrates with blade coated charge transporting layers in ambient air and green solvents, namely de-ionized water for SnO₂ and p-Xylene for Spiro-OMeTAD⁴². We use phenethylammonium iodide (PEAI) to passivate the perovskite layer⁴³. **Figure 4a** shows a SEM cross-section image and **Figure S12** the XRD pattern of the device. The J-V measurement of the champion device reveals negligible hysteresis with an open-circuit voltage (V_{OC}) of 1.11 V, a short-circuit current density (J_{SC}) of 23.31 mA/cm² and a fill factor (FF) of 72.00 %, resulting in a PCE of 18.66 % (**Figure 4b**). The maximum power point (MPP) tracking yields 17.74 mW/cm² after 30 s (**Figure 4c**). This is the highest value for fully scalable PSCs with green solvents (**Figure 4d**). Additionally, we provide photovoltaic performance statistics of 34 cells on 5 cm x 5 cm substrates to show the uniformity of the process (**Figure S13**). On average, we obtain a V_{OC} of around 1.13 V and J_{SC} of 21 mA/cm². The best device showed V_{OC} of 1.16 V for a bandgap of 1.56 eV, being only limited by FF and J_{SC} . The external quantum efficiency (EQE) measurement yields integrated J_{SC} value of 21.86 mA/cm², showing further scope of improvement in the light management (**Figure S14**).

In conclusion, we report a new and scalable hybrid perovskite fabrication process, combining thermal evaporation and blade coating using non-toxic solvents. We systematically investigate the influence of processing parameters on the perovskite formation mechanism during the PVD/blade process and elucidate the growth mechanism. We use such perovskite absorbers together with ambient air-processed, blade coated charge transporting layers to fabricate scalable PSCs with V_{OC} of 1.16 V and PCE up to 18.7 % using green solvents only. With our work, we make an important contribution to reduce the performance gap between toxic and green solvent-based, scalable perovskite fabrication. PVD/blade is a promising process to fabricate high quality perovskite layers

on large-area substrates. It can allow a facile implementation of passivation strategies and additives into the perovskite absorber. Additionally, it can be adapted for wide bandgap perovskite films and be eventually applied to coat textured surfaces, e.g. in tandem solar cell applications. Moreover, other meniscus-guided deposition methods can replace blade coating, such as slot-die coating or inkjet printing on flexible foils, paving the way for roll-to-roll or sheet-to-sheet manufacturing. Overall, the proposed method and its variants are easily scalable for large area manufacturing while the avoidance of toxic solvents is an additional advantage for successful commercialization of PSC technology.

ASSOCIATED CONTENT

Supporting Information. Additional notes on inorganic halide template and two-step fabrication methods, XRD patterns, AFM images, SEM cross-section view images, τ_{auc} and absorption coefficient plots, table of TRPL decay lifetimes and reference list to chart.

Notes

The authors declare no competing financial interest.

ACKNOWLEDGMENT

This work has received funding from the European Union's Horizon 2020 research and innovation program under grant agreement No. 850937 of the PERCISTAND project, the Swiss Federal Office of Energy (SFOE, Project CIGSPSC, grant no. SI/501805-01), and the Swiss National Science Foundation (SNF, Project Bridge Power, grant no. 176552).

REFERENCES

- (1) Green, M. A.; Emery, K. Solar Cell Efficiency Tables. *Prog. Photovoltaics Res. Appl.* **1993**, *1* (1), 25–29. <https://doi.org/10.1002/pip.4670010104>.
- (2) De Wolf, S.; Holovsky, J.; Moon, S. J.; Löper, P.; Niesen, B.; Ledinsky, M.; Haug, F. J.; Yum, J. H.; Ballif, C. Organometallic Halide Perovskites: Sharp Optical Absorption Edge and Its Relation to Photovoltaic Performance. *J. Phys. Chem. Lett.* **2014**, *5* (6), 1035–1039. <https://doi.org/10.1021/jz500279b>.
- (3) Eperon, G. E.; Stranks, S. D.; Menelaou, C.; Johnston, M. B.; Herz, L. M.; Snaith, H. J. Formamidinium Lead Trihalide: A Broadly Tunable Perovskite for Efficient Planar Heterojunction Solar Cells. *Energy Environ. Sci.* **2014**, *7* (3), 982–988. <https://doi.org/10.1039/c3ee43822h>.
- (4) Dong, Q. Electron-Hole Diffusion Lengths $> 175 \mu\text{m}$ in Solution-Grown $\text{CH}_3\text{NH}_3\text{PbI}_3$ Single Crystals. *Science (80-.)*. **2015**, *347* (6225).
- (5) Kovalenko, M. V.; Protesescu, L.; Bodnarchuk, M. I. Properties and Potential Optoelectronic Applications of Lead Halide Perovskite Nanocrystals. *Science (80-.)*. **2017**, *358* (6364), 745–750. <https://doi.org/10.1126/science.aam7093>.
- (6) Yin, W. J.; Shi, T.; Yan, Y. Unusual Defect Physics in $\text{CH}_3\text{NH}_3\text{PbI}_3$ Perovskite Solar Cell Absorber. *Appl. Phys. Lett.* **2014**, *104* (6). <https://doi.org/10.1063/1.4864778>.
- (7) Lee, M. M.; Teuscher, J.; Miyasaka, T.; Murakami, T. N.; Snaith, H. J. Efficient Hybrid Solar Cells Based on Meso-Superstructured Organometal Halide Perovskites. *Science (80-.)*. **2012**, *338* (6107), 643–647. <https://doi.org/10.1126/science.1228604>.
- (8) Deng, Y.; Peng, E.; Shao, Y.; Xiao, Z.; Dong, Q.; Huang, J. Scalable Fabrication of Efficient Organolead Trihalide Perovskite Solar Cells with Doctor-Bladed Active Layers. *Energy*

- Environ. Sci.* **2015**, 8 (5), 1544–1550. <https://doi.org/10.1039/c4ee03907f>.
- (9) Razza, S.; Di Giacomo, F.; Matteocci, F.; Cinà, L.; Palma, A. L.; Casaluci, S.; Cameron, P.; D'Epifanio, A.; Licoccia, S.; Reale, A.; Brown, T. M.; Di Carlo, A. Perovskite Solar Cells and Large Area Modules (100 Cm²) Based on an Air Flow-Assisted PbI₂ Blade Coating Deposition Process. *J. Power Sources* **2015**, 277, 286–291. <https://doi.org/10.1016/j.jpowsour.2014.12.008>.
- (10) Hwang, K.; Jung, Y. S.; Heo, Y. J.; Scholes, F. H.; Watkins, S. E.; Subbiah, J.; Jones, D. J.; Kim, D. Y.; Vak, D. Toward Large Scale Roll-to-Roll Production of Fully Printed Perovskite Solar Cells. *Adv. Mater.* **2015**, 27 (7), 1241–1247. <https://doi.org/10.1002/adma.201404598>.
- (11) Vak, D.; Hwang, K.; Faulks, A.; Jung, Y. S.; Clark, N.; Kim, D. Y.; Wilson, G. J.; Watkins, S. E. 3D Printer Based Slot-Die Coater as a Lab-to-Fab Translation Tool for Solution-Processed Solar Cells. *Adv. Energy Mater.* **2015**, 5 (4), 1–8. <https://doi.org/10.1002/aenm.201401539>.
- (12) Wei, Z.; Chen, H.; Yan, K.; Yang, S. Inkjet Printing and Instant Chemical Transformation of a CH₃NH₃PbI₃/Nanocarbon Electrode and Interface for Planar Perovskite Solar Cells. *Angew. Chemie - Int. Ed.* **2014**, 53 (48), 13239–13243. <https://doi.org/10.1002/anie.201408638>.
- (13) Heo, J. H.; Lee, M. H.; Jang, M. H.; Im, S. H. Highly Efficient CH₃NH₃PbI₃-xCl_x Mixed Halide Perovskite Solar Cells Prepared by Re-Dissolution and Crystal Grain Growth via Spray Coating. *J. Mater. Chem. A* **2016**, 4 (45), 17636–17642. <https://doi.org/10.1039/c6ta06718b>.
- (14) Jeong, J.; Kim, M. M.; Seo, J.; Lu, H.; Ahlawat, P.; Mishra, A.; Yang, Y.; Hope, M. A.;

- Eickemeyer, F. T.; Kim, M. M.; Yoon, Y. J.; Choi, I. W.; Darwich, B. P.; Choi, S. J.; Jo, Y.; Lee, J. H.; Walker, B.; Zakeeruddin, S. M.; Emsley, L.; Rothlisberger, U.; Hagfeldt, A.; Kim, D. S.; Grätzel, M.; Kim, J. Y. Pseudo-Halide Anion Engineering for α -FAPbI₃ Perovskite Solar Cells. *Nature* **2021**, *592* (April). <https://doi.org/10.1038/s41586-021-03406-5>.
- (15) Deng, Y.; Zheng, X.; Bai, Y.; Wang, Q.; Zhao, J.; Huang, J. Surfactant-Controlled Ink Drying Enables High-Speed Deposition of Perovskite Films for Efficient Photovoltaic Modules. *Nat. Energy* **2018**, *3* (7), 560–566. <https://doi.org/10.1038/s41560-018-0153-9>.
- (16) Wu, W. Q.; Yang, Z.; Rudd, P. N.; Shao, Y.; Dai, X.; Wei, H.; Zhao, J.; Fang, Y.; Wang, Q.; Liu, Y.; Deng, Y.; Xiao, X.; Feng, Y.; Huang, J. Bilateral Alkylamine for Suppressing Charge Recombination and Improving Stability in Blade-Coated Perovskite Solar Cells. *Sci. Adv.* **2019**, *5* (3), 1–10. <https://doi.org/10.1126/sciadv.aav8925>.
- (17) Di Giacomo, F.; Shanmugam, S.; Fledderus, H.; Bruijnaers, B. J.; Verhees, W. J. H.; Dorenkamper, M. S.; Veenstra, S. C.; Qiu, W.; Gehlhaar, R.; Merckx, T.; Aernouts, T.; Andriessen, R.; Galagan, Y. Up-Scalable Sheet-to-Sheet Production of High Efficiency Perovskite Module and Solar Cells on 6-in. Substrate Using Slot Die Coating. *Sol. Energy Mater. Sol. Cells* **2018**, *181* (August 2017), 53–59. <https://doi.org/10.1016/j.solmat.2017.11.010>.
- (18) Tang, S.; Deng, Y.; Zheng, X.; Bai, Y.; Fang, Y.; Dong, Q.; Wei, H.; Huang, J. Composition Engineering in Doctor-Blading of Perovskite Solar Cells. *Adv. Energy Mater.* **2017**, *7* (18), 1–7. <https://doi.org/10.1002/aenm.201700302>.
- (19) Wu, W. Q.; Wang, Q.; Fang, Y.; Shao, Y.; Tang, S.; Deng, Y.; Lu, H.; Liu, Y.; Li, T.; Yang, Z.; Gruverman, A.; Huang, J. Molecular Doping Enabled Scalable Blading of Efficient

- Hole-Transport-Layer-Free Perovskite Solar Cells. *Nat. Commun.* **2018**, 9 (1), 1–8. <https://doi.org/10.1038/s41467-018-04028-8>.
- (20) Deng, Y.; van Brackle, C. H.; Dai, X.; Zhao, J.; Chen, B.; Huang, J. Tailoring Solvent Coordination for High-Speed, Room-Temperature Blading of Perovskite Photovoltaic Films. *Sci. Adv.* **2019**, 5 (12), 1–9. <https://doi.org/10.1126/sciadv.aax7537>.
- (21) Chen, S.; Dai, X.; Xu, S.; Jiao, H.; Zhao, L.; Huang, J. Stabilizing Perovskite-Substrate Interfaces for High-Performance Perovskite Modules. **2021**, 907 (August), 902–907.
- (22) Michael M. Lee, Joël Teuscher, Tsutomu Miyasaka, Takuro N. Murakami, H. J. S. Efficient Hybrid Solar Cells Based on Meso-Superstructured Organometal Halide Perovskites. **2012**, 338 (6107), 643–647. <https://doi.org/10.1126/science.1228604>.
- (23) National Center for Biotechnology Information. 2-Methoxyethanol - PubChem Compound Summary for CID 8019 - <https://pubchem.ncbi.nlm.nih.gov/compound/2-Methoxyethanol> (accessed Jun 18, 2021).
- (24) National Center for Biotechnology Information. N,N-Dimethylformamide - PubChem Compound Summary for CID 8019 <https://pubchem.ncbi.nlm.nih.gov/compound/6228> (accessed Jun 18, 2021).
- (25) Park, N. G. Green Solvent for Perovskite Solar Cell Production. *Nat. Sustain.* **2021**, 4 (3), 192–193. <https://doi.org/10.1038/s41893-020-00647-6>.
- (26) Sahli, F.; Werner, J.; Kamino, B. A.; Bräuninger, M.; Monnard, R.; Paviet-Salomon, B.; Barraud, L.; Ding, L.; Diaz Leon, J. J.; Sacchetto, D.; Cattaneo, G.; Despeisse, M.; Boccard, M.; Nicolay, S.; Jeangros, Q.; Niesen, B.; Ballif, C. Fully Textured Monolithic Perovskite/Silicon Tandem Solar Cells with 25.2% Power Conversion Efficiency. *Nat. Mater.* **2018**, 17 (9), 820–826. <https://doi.org/10.1038/s41563-018-0115-4>.

- (27) Jošt, M.; Kegelman, L.; Korte, L.; Albrecht, S. Monolithic Perovskite Tandem Solar Cells: A Review of the Present Status and Advanced Characterization Methods Toward 30% Efficiency. *Adv. Energy Mater.* **2020**, *10* (26). <https://doi.org/10.1002/aenm.201904102>.
- (28) Momblona, C.; Gil-Escrig, L.; Bandiello, E.; Hutter, E. M.; Sessolo, M.; Lederer, K.; Blochwitz-Nimoth, J.; Bolink, H. J. Efficient Vacuum Deposited P-i-n and n-i-p Perovskite Solar Cells Employing Doped Charge Transport Layers. *Energy Environ. Sci.* **2016**, *9* (11), 3456–3463. <https://doi.org/10.1039/c6ee02100j>.
- (29) Ávila, J.; Momblona, C.; Boix, P. P.; Sessolo, M.; Bolink, H. J. Vapor-Deposited Perovskites: The Route to High-Performance Solar Cell Production? *Joule* **2017**, *1* (3), 431–442. <https://doi.org/10.1016/j.joule.2017.07.014>.
- (30) Köhnen, E.; Wagner, P.; Lang, F.; Cruz, A.; Li, B.; Roß, M.; Jošt, M.; Morales-Vilches, A. B.; Topič, M.; Stolterfoht, M.; Neher, D.; Korte, L.; Rech, B.; Schlattmann, R.; Stannowski, B.; Albrecht, S. 27.9% Efficient Monolithic Perovskite/Silicon Tandem Solar Cells on Industry Compatible Bottom Cells. *Sol. RRL* **2021**, *2100244*, 1–8. <https://doi.org/10.1002/solr.202100244>.
- (31) Li, J.; Wang, H.; Chin, X. Y.; Dewi, H. A.; Vergeer, K.; Goh, T. W.; Lim, J. W. M.; Lew, J. H.; Loh, K. P.; Soci, C.; Sum, T. C.; Bolink, H. J.; Mathews, N.; Mhaisalkar, S.; Bruno, A. Highly Efficient Thermally Co-Evaporated Perovskite Solar Cells and Mini-Modules. *Joule* **2020**, *4* (5), 1035–1053. <https://doi.org/10.1016/j.joule.2020.03.005>.
- (32) Feng, J.; Jiao, Y.; Wang, H.; Zhu, X.; Sun, Y.; Du, M.; Cao, Y.; Yang, D.; Liu, S. (Frank). High-Throughput Large-Area Vacuum Deposition for High-Performance Formamidine-Based Perovskite Solar Cells. *Energy Environ. Sci.* **2021**, *14* (5), 3035–3043. <https://doi.org/10.1039/d1ee00634g>.

- (33) Gil-Escrig, L.; Momblona, C.; La-Placa, M. G.; Boix, P. P.; Sessolo, M.; Bolink, H. J. Vacuum Deposited Triple-Cation Mixed-Halide Perovskite Solar Cells. *Adv. Energy Mater.* **2018**, *8* (14), 1–6. <https://doi.org/10.1002/aenm.201703506>.
- (34) Bing, J.; Huang, S.; Ho-Baillie, A. W. Y. A Review on Halide Perovskite Film Formation by Sequential Solution Processing for Solar Cell Applications. *Energy Technol.* **2020**, *8* (4), 1–22. <https://doi.org/10.1002/ente.201901114>.
- (35) Liu, D.; Gangishetty, M. K.; Kelly, T. L. Effect of CH₃NH₃PbI₃ Thickness on Device Efficiency in Planar Heterojunction Perovskite Solar Cells. *J. Mater. Chem. A* **2014**, *2* (46), 19873–19881. <https://doi.org/10.1039/c4ta02637c>.
- (36) Ummadisingu, A.; Grätzel, M. Revealing the Detailed Path of Sequential Deposition for Metal Halide Perovskite Formation. *Sci. Adv.* **2018**, *4* (2), 1–10. <https://doi.org/10.1126/sciadv.1701402>.
- (37) Stoumpos, C. C.; Malliakas, C. D.; Kanatzidis, M. G. Semiconducting Tin and Lead Iodide Perovskites with Organic Cations: Phase Transitions, High Mobilities, and near-Infrared Photoluminescent Properties. *Inorg. Chem.* **2013**, *52* (15), 9019–9038. <https://doi.org/10.1021/ic401215x>.
- (38) Gu, X.; Shaw, L.; Gu, K.; Toney, M. F.; Bao, Z. The Meniscus-Guided Deposition of Semiconducting Polymers. *Nat. Commun.* **2018**, *9* (1). <https://doi.org/10.1038/s41467-018-02833-9>.
- (39) Fu, F.; Kranz, L.; Yoon, S.; Löckinger, J.; Jäger, T.; Perrenoud, J.; Feurer, T.; Gretener, C.; Buecheler, S.; Tiwari, A. N. Controlled Growth of PbI₂ Nanoplates for Rapid Preparation of CH₃NH₃PbI₃ in Planar Perovskite Solar Cells. *Phys. Status Solidi Appl. Mater. Sci.* **2015**, *212* (12), 2708–2717. <https://doi.org/10.1002/pssa.201532442>.

- (40) Zanatta, A. R. Revisiting the Optical Bandgap of Semiconductors and the Proposal of a Unified Methodology to Its Determination. *Sci. Rep.* **2019**, *9* (1), 11225. <https://doi.org/10.1038/s41598-019-47670-y>.
- (41) Yamada, Y.; Nakamura, T.; Endo, M.; Wakamiya, A.; Kanemitsu, Y. Photocarrier Recombination Dynamics in Perovskite CH₃NH₃PbI₃ for Solar Cell Applications. *J. Am. Chem. Soc.* **2014**, *136* (33), 11610–11613. <https://doi.org/10.1021/ja506624n>.
- (42) Isabelli, F.; Di Giacomo, F.; Gortler, H.; Brunetti, F.; Groen, P.; Andriessen, R.; Galagan, Y. Solvent Systems for Industrial-Scale Processing of Spiro-OMeTAD Hole Transport Layer in Perovskite Solar Sells. *ACS Appl. Energy Mater.* **2018**, *1* (11), 6056–6063. <https://doi.org/10.1021/acsaem.8b01122>.
- (43) Jiang, Q.; Zhao, Y.; Zhang, X.; Yang, X.; Chen, Y.; Chu, Z.; Ye, Q.; Li, X.; Yin, Z.; You, J. Surface Passivation of Perovskite Film for Efficient Solar Cells. *Nat. Photonics* **2019**, *13* (7), 460–466. <https://doi.org/10.1038/s41566-019-0398-2>.

SUPPLEMENTARY INFORMATION

Triple-cation perovskite solar cells fabricated by hybrid PVD/blade coating process using green solvents

*Severin Siegrist, Shih-Chi Yang, Evgeniia Gilshtein, Xiaoxiao Sun, Ayodhya N. Tiwari and Fan Fu**

Laboratory for Thin Films and Photovoltaics, Empa – Swiss Federal Laboratories for Materials Science and Technology, Ueberlandstrasse 129, 8600 Duebendorf, Switzerland

*Email: fan.fu@empa.ch

EXPERIMENTAL SECTION

Perovskite film by PVD/blade: The inorganic halide template was sequentially deposited in a high-vacuum ($< 6 \times 10^{-6}$ mbar), in-house developed thermal evaporator. First, 15 nm of CsI (> 99 %, TCI) was evaporated with 0.1 nm/s, followed by 300 nm of PbI_2 (> 99 %, TCI) with 0.7 nm/s. Next, the organic halide precursors, formamidinium iodide (FAI, > 99.99 % , greatcellsolar), methylammonium bromide (MABr, > 99.99 %, greatcellsolar) and methylammonium chloride (MACl, > 99.0 %, Sigma-Aldrich) were mixed according to FAI/MABr/MACl 60/6/6 mg in 1ml isopropanol. The mixed solution was blade coated with 30 mm/s at 65 °C and with a gap of 100 μm in ambient air, followed by 15 min annealing at 150 °C in ambient air (~ 35 % relative humidity).

Perovskite film by Spin + Spin: The inorganic halide template was deposited by spin coating 1.3 M of PbI_2 (> 99 %, TCI) and 0.065 M of CsI (> 99 %, TCI) dissolved in mixed N,N-dimethylformamide (DMF, 99.8 %, Sigma-Aldrich) and dimethyl sulfoxide (DMSO, ≥ 99.9 %) with volume ratio of 9:1 at 1500 r.p.m. for 30 s and annealed at 70 °C for 1 min inside the glovebox. Next, the organic halide precursors, formamidinium iodide (FAI, > 99.99 % , greatcellsolar), methylammonium bromide (MABr, > 99.99 %, greatcellsolar) and methylammonium chloride (MACl, > 99.0 %, Sigma-Aldrich) were mixed according to FAI/MABr/MACl 60/6/6 mg in 1ml isopropanol. The mixed solution was spin coated with 1300 r.p.m. for 40 s in the glovebox, followed by 15 min annealing at 150 °C in ambient air (~ 35 % relative humidity).

Solar cell fabrication: The solar cell was fabricated with a layer structure of IOH/ SnO_2 /perovskite/PEAI/Spiro-OMeTAD/Au. First, hydrogenated indium oxide (IOH) with a sheet resistance of $10 \Omega/\text{sq}$ were deposited on cleaned soda-lime glass substrates in a high-vacuum sputtering system (CT200, Allianceconcept) by RF sputtering of ceramic In_2O_3 targets (99.99 %,

10 in. diameter, SPM AG) in a mixed Ar, O₂, and H₂ atmosphere at room temperature according to Yang et al.⁶⁴. Afterwards, the IOH film was annealed at 200 °C for 20 min in ambient air (35 - 40 % rel. humidity). Oxygen plasma treatment was performed for 5 min on the substrate before blade coating the electron transporting layer (ETL). SnO₂ colloid precursor (15 wt% in H₂O colloidal dispersion, Alfa Aesar) was diluted in de-ionized water 1:3 by volume and blade coated with 30 mm/s at 70 °C and a gap between blade and substrate of 100 μm in ambient air. The SnO₂ was annealed at 150 °C for 30 min in ambient air. The perovskite with thickness around 560 nm was deposited on top of the ETL via one of the indicated two-step fabrication methods. After perovskite formation, 5 mg of phenethylammonium iodide (PEAI, 98 %, Sigma-Aldrich) per ml of isopropanol was spin coated onto the perovskite film with a spin rate of 5000 r.p.m. Next, the hole transporting layer Spiro-OMeTAD layer was blade coated with 90 mm/s at 40 °C and with a gap of 100 μm in ambient air on top of perovskite layer with a solution that contained 25 mg 2,2',7,7'-tetrakis-(N,N'-di-p-methoxyphenylamine)-9,9'-spirobifluorene (Xi'an Polymer Light Technology), 10 μl of 4-tert-butylpyridine (98 %, Sigma-Aldrich) and 6 μl of lithium bis(trifluoromethanesulfonyl)imide (Li-TFSI) solution (520 mg of Li-TFSI (99 %, Sigma-Aldrich) in 1 ml of acetonitrile (99.8 %, Sigma-Aldrich)) in 1 ml of p-Xylene (≥ 99 %, Sigma-Aldrich). Finally, 80 nm Au back electrode was thermally evaporated with 0.15 nm/s at a base pressure of 6×10^{-6} mbar.

Solar cell performance characterizations: Photocurrent–voltage (J–V) characteristics were measured in four-contact mode at standard test conditions (100 mWcm⁻²) using a Keithley 2400 source meter. A solar simulator (ABA class, LOT-QuantumDesign) was calibrated using a certified monocrystalline silicon solar cell (RS-ID-5, Fraunhofer-ISE) and was used to simulate the AM 1.5 G one sun illumination. Illumination is in superstrate configuration without external

cooling of the sample. The active area is 0.1 cm^2 of each pixel, defined by the mask of the gold electrode. The J–V measurements were performed in both forward (from -0.2 to 1.2 V) and backward (from 1.2 to -0.2 V) directions in ambient air ($\sim 40 \%$ relative humidity) at room temperature. No pretreatment, e.g., bias or illumination, was applied before measurement. The steady-state efficiency as a function of time was recorded using a maximum power point tracker, which adjusts the applied voltage in order to reach the maximum power point (perturb and observe algorithm). The external quantum efficiency of the devices were measured with a lock-in amplifier. The probing beam was generated by a chopped white source (900W, halogen lamp, 280 Hz) and a dual grating monochromator. The beam size was adjusted to ensure that the illumination area was fully inside the cell area. A certified single crystalline silicon solar cell was used as a reference cell. White light bias was applied during the measurement with ~ 0.1 sun intensity.

Material characterizations

ToF-SIMS: Element depth profiles were obtained with a time-of-flight secondary ion mass spectrometer (ToF.SIMS V system, ION-TOF). The primary beam was 25 keV Bi^{3+} with a total current of 0.22 pA and a raster size of $50 \times 50 \text{ }\mu\text{m}^2$. For detection of negative ions, Cs^+ ions were used with 500 eV ion energy, 25 nA pulse current on a $300 \times 300 \text{ }\mu\text{m}^2$ raster size to bombard and etch the film. For detection of positive ions, sputtering was performed using O_2^- ions at 2 keV ion energy, 180 nA pulse current over a raster size of $300 \times 300 \text{ }\mu\text{m}^2$. The data were plotted with the intensity for each signal normalized to the total counts of the signal.

XPS. X-ray photoelectron spectroscopy was performed using a Quantum 2000 system from Physical Electronics with a monochromatic Al K_α source (1486.6 eV, spot size, $100 \text{ }\mu\text{m}$) and a base pressure below 8×10^{-8} mbar. No surface cleaning was performed. Detailed high-resolution scans

of I 3d, S 2p, N 1s, Cl 2p, O 1s, Br 3d, C 1s, Cs 3d, Pb 4f were recorded with an energy step size of 0.125 eV and a pass energy of 29.35 eV during depth profile sputtering by Ar⁺ sputtering. The first five cycles (with the first measurement performed directly on the surface) were performed with 0.5 kV energy after 30 s sputtering each, followed by five more cycles: three with 2 min intervals and 2 more with 4 min intervals with the same energy. The sputtering rate was estimated to be around 15-20 nm/min which corresponds to 250-300 nm total depth of the performed analysis. With the use of MultiPak processing software all data were background subtracted.

TRPL/PL: Time-resolved photoluminescence (TRPL) and steady-state photoluminescence (PL) were measured using a FluoTime 300 unit coupled into a MicroTime 100 system from PicoQuant. For TRPL measurement, a 639 nm pulsed laser with < 100 ps pulse width was used as an excitation source. The spot size was measured using a NanoScan2 beam profiler resulting in ~ 130 mm diameter. The excitation was 3×10^{11} photons cm⁻² pulse⁻¹ and the pulse frequency was 0.1 MHz. For the fitting procedure, a bi-exponential decay was used and the first 20 ns after the signal peak were neglected.

AFM: The AFM characterization was carried out using an AFM microscope (Bruker ICON3) in the air. A silicon nitride tip (ScanAsyst-air) with a radius of 10 nm was used as the probe. The cantilevers' spring constant and resonant frequency are 0.4 N/m and 70 kHz, respectively.

UV-Vis: Reflectance and transmittance measurements were performed using a Shimadzu UV-Vis 3600 spectrophotometer equipped with an integrating sphere. The reflectance data were corrected for the instrumental response stemming from diffuse and specular reflections both on the sample, and the reflectance measurements were carried out in a wavelength range from 300 to 1500 nm.

XRD: X-Ray diffraction patterns were measured on an X'Pert Pro in Bragg–Brentano geometry using Cu K α_1 radiation ($\lambda = 1.5406 \text{ \AA}$), scanning from 5 to 60 ° (2θ) with a step interval of 0.0167°.

SEM: The SEM micrographs were taken with a Hitachi S-4800 Scanning Electron Microscope using 5–10 kV acceleration voltage. A thin layer (1 nm) of Pt was coated on top of the samples to avoid charging effects.

NOTES

Note S1: Morphology of inorganic halide template with different amorphous substrates

Fu et al. have shown that the crystal characteristics of the substrate influence the morphology of the evaporated inorganic template¹. While amorphous substrates yield in compact PbI₂ layers, poly-crystalline substrates lead to porous, plate-like PbI₂ layers. We use this finding to deposit perovskite films on amorphous substrates to avoid further material restrictions for the perovskite fabrication method by PVD/blade. We provide SEM cross-section images of the inorganic halide template on different amorphous materials, including a) soda-lime glass (SLG), b) IOH and c) colloidal SnO₂ nanocrystals to support the versatility of this method. As depicted in **Figure S15c-d**, the morphology of the evaporated inorganic halide template is similar for each of these substrates and in all cases, we obtain a compact inorganic template. Additionally, the XRD spectra of these films show a comparable crystallinity of the evaporated inorganic template with a preferred orientation of (001) plane over (101) (**Figure S15a**). Therefore, we assume a similar infiltration mechanism for the organic halide precursor solution into the inorganic halide template. Hence, we expect a comparable perovskite film formation by PVD/blade for any amorphous substrate, including inert quartz.

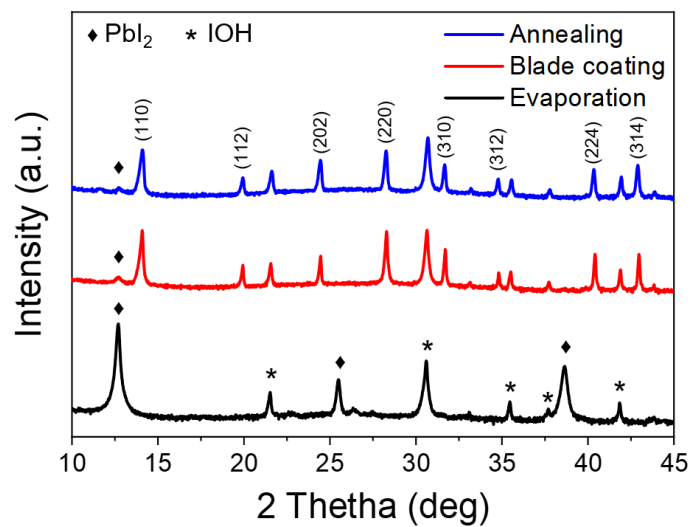


Figure S1: XRD patterns (log-scale) of the film after thermal evaporation, blade coating and annealing with indicated perovskite crystal plane orientations. PbI_2 is labeled by ◆ and IOH by *.

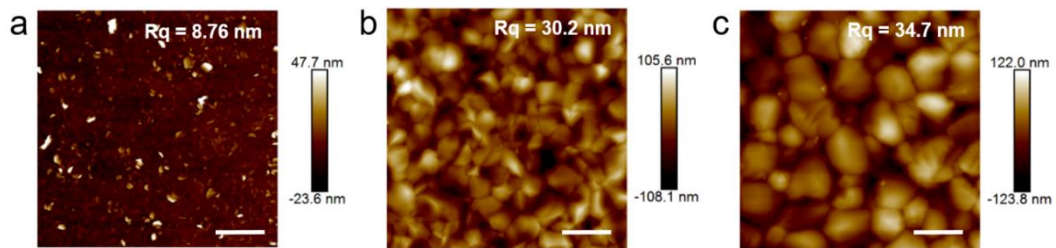


Figure S2: AFM height images of the film surface after a) evaporation, b) blade coating and c) annealing. The scale bar is 1 μm.

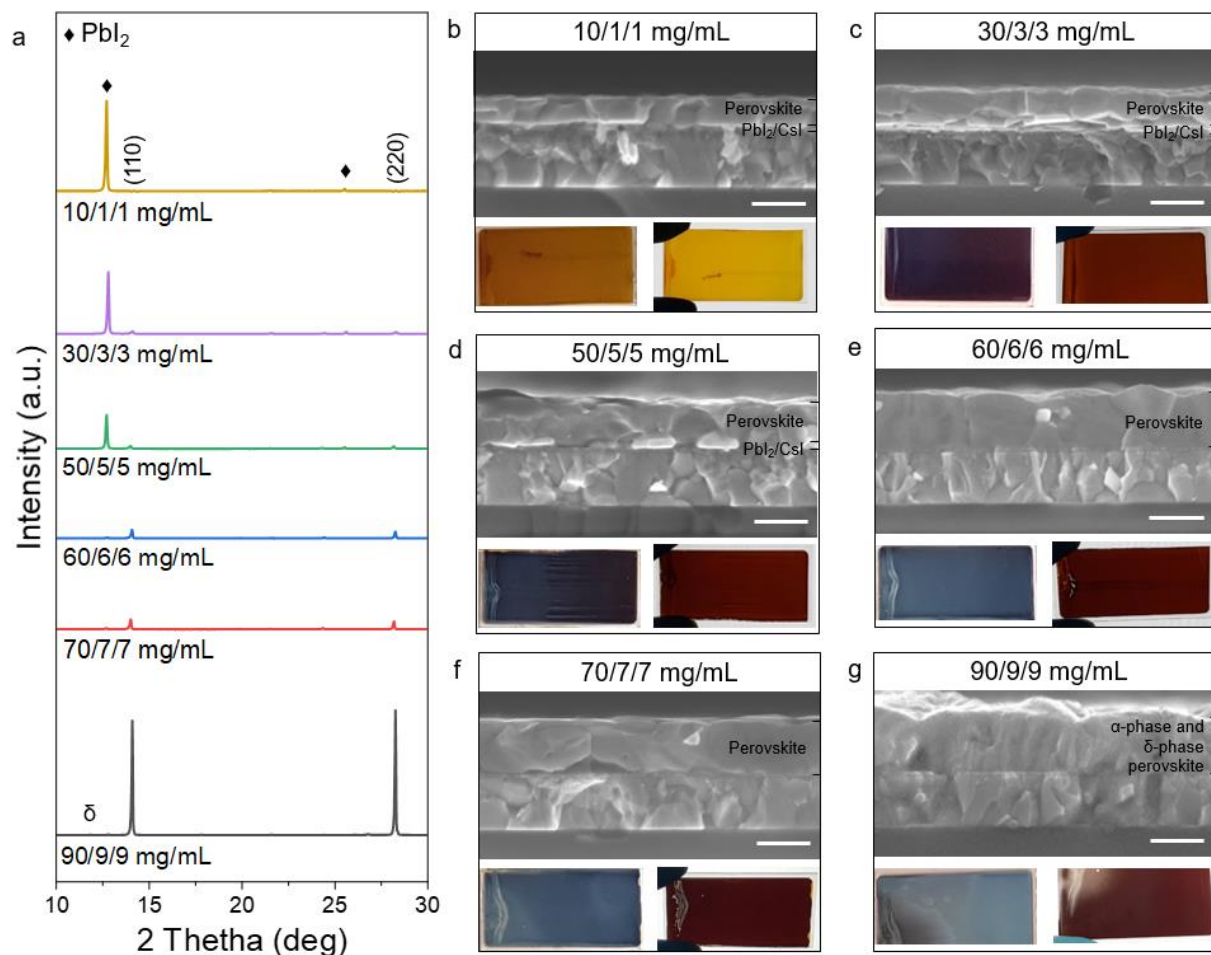


Figure S3: Perovskite films fabricated with different concentrations of the organic halide precursors (FAI/MABr/MACl in mg/mL) in the solution. a) XRD pattern with indicated diffraction peaks of the α -phase perovskite crystal planes. The δ -phase perovskite is labeled by δ and PbI_2 by \diamond . b-g) SEM cross-section view images for each concentration with sample pictures taken in foreground and in background illumination mode. The scale bar is 500 nm.

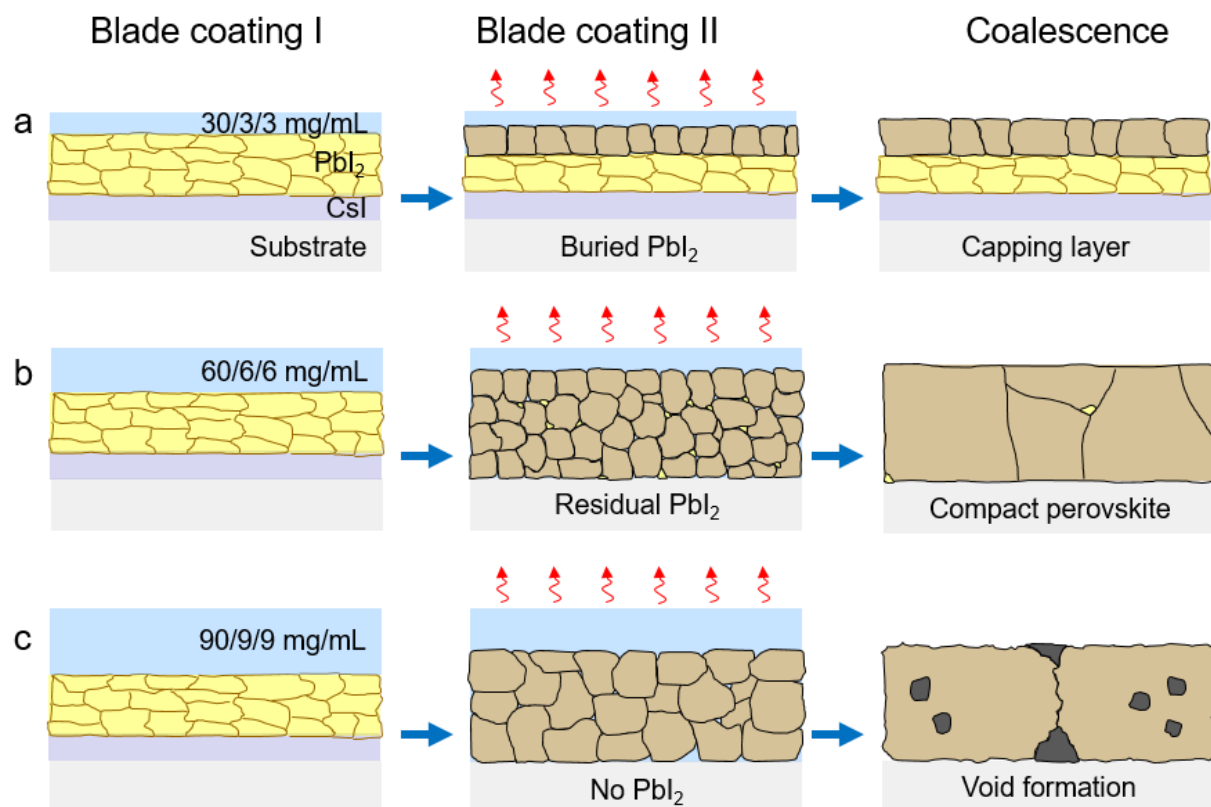


Figure S4: Influence of organic halide precursor concentration on the degree of perovskite conversion of the film. a) Formation of perovskite capping layer when blade coating of 30/3/3 mg/mL FAI/MABr/MACl on the inorganic halide template. b) Almost fully converted perovskite film with unreacted PbI_2 residues for 60/6/6 mg/mL. c) Formation of defective, but highly crystalline perovskite film with voids in the bulk and rough crystal grains, when using 90/9/9 mg/mL of organic halide precursors. The amount of organic halide precursors is represented by the solution thickness (blue).

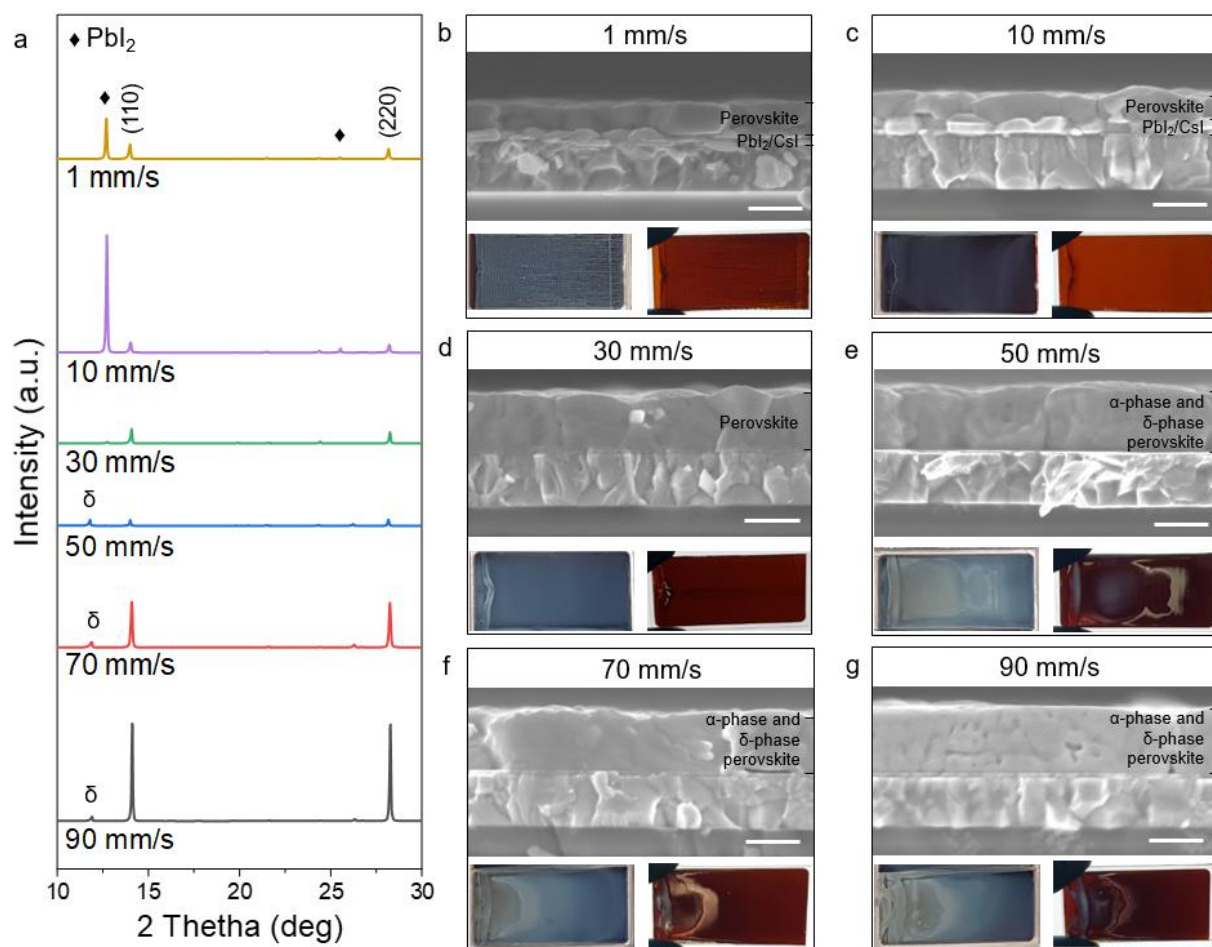


Figure S5: Perovskite films fabricated with different blading speeds. a) XRD pattern with indicated diffraction peaks of the α -phase perovskite crystal planes. The δ -phase perovskite is labeled by δ and PbI_2 by \diamond . b-g) SEM cross-section view images for each speed with sample pictures taken in foreground and in background illumination mode. The scale bar is 500 nm.

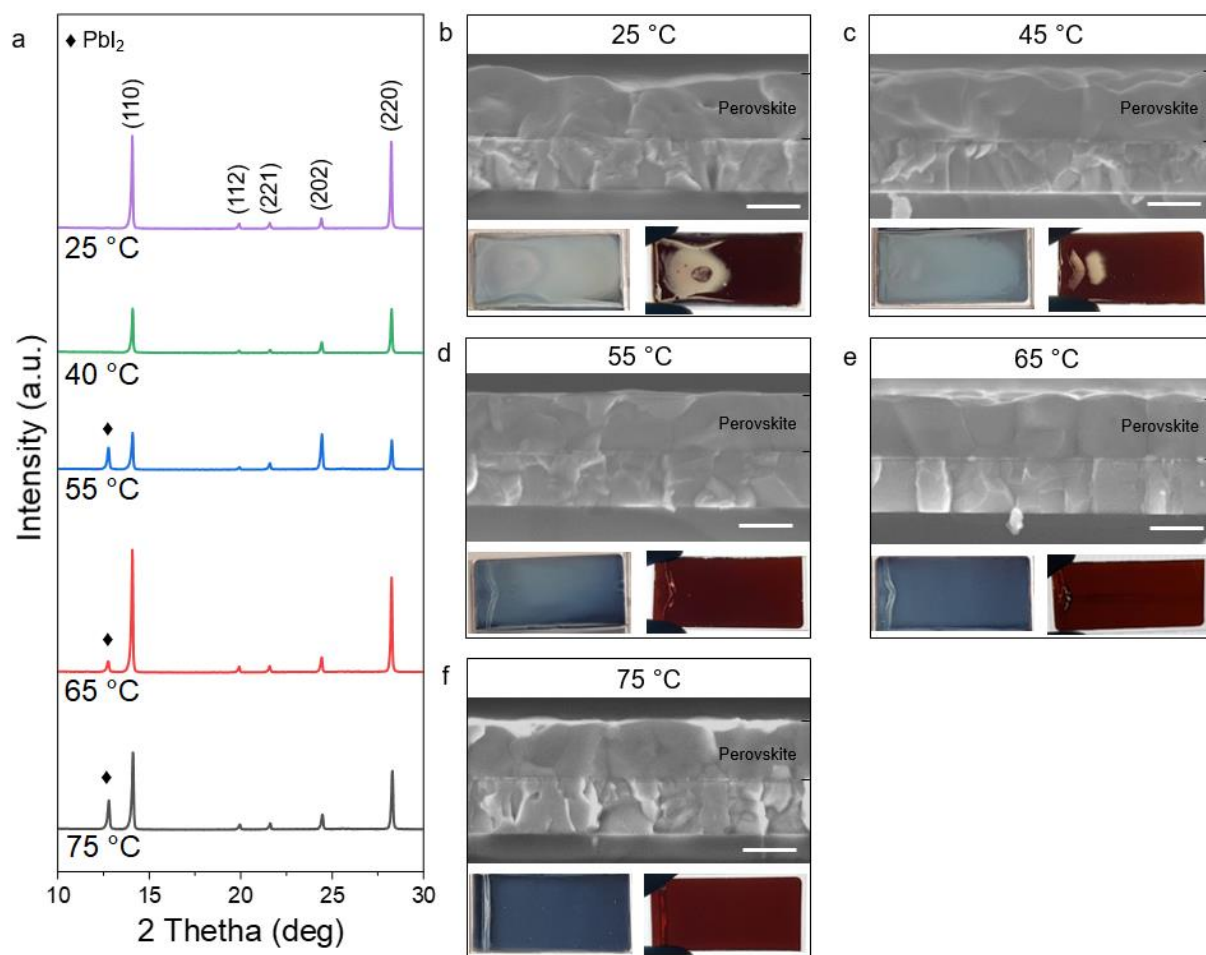


Figure S6: Perovskite films fabricated at different substrate temperatures. a) XRD pattern with indicated diffraction peaks of the α -phase perovskite crystal planes. PbI_2 is labeled by \blacklozenge . b-f) SEM cross-section view images for each substrate temperature with sample pictures taken in foreground and in background illumination mode. The scale bar is 500 nm.

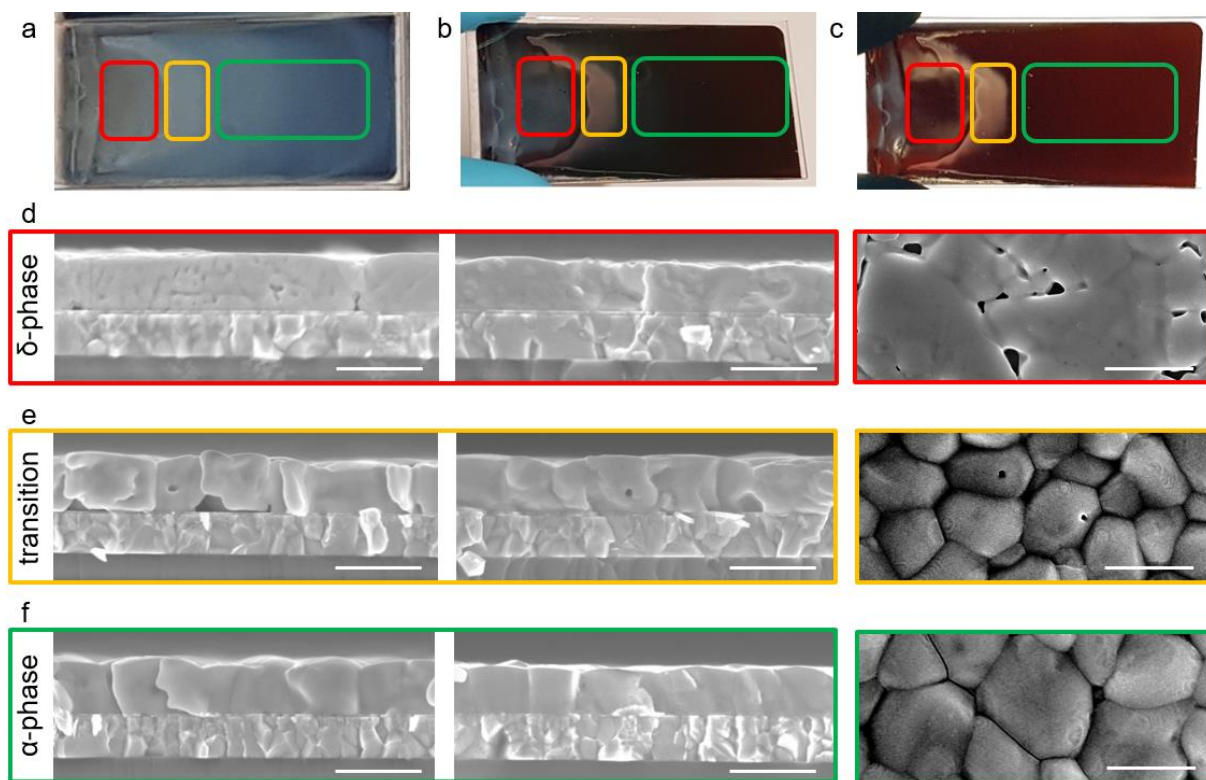


Figure S7: Perovskite crystal phases and morphology that occur, when the processing parameters are not matching, i.e. the balance of inorganic halide precursors and organic halide precursors is not given. Sample pictures of the perovskite film blade coated with 70 mm/s at 65 °C with an organic halide concentration of 60/6/6 mg/mL of FAI/MABr/MACl in foreground illumination mode: a) front side and b) backside of the sample as well as in c) background illumination mode. SEM cross-section and top view images of the d) δ -phase perovskite region, e) transition region and f) α -phase perovskite region. The scale bar is 1 μm .

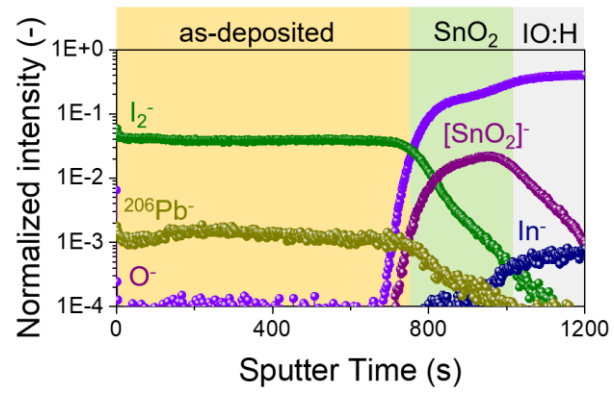


Figure S8: ToF-SIMS depth profile of negative species of the as-deposited film.

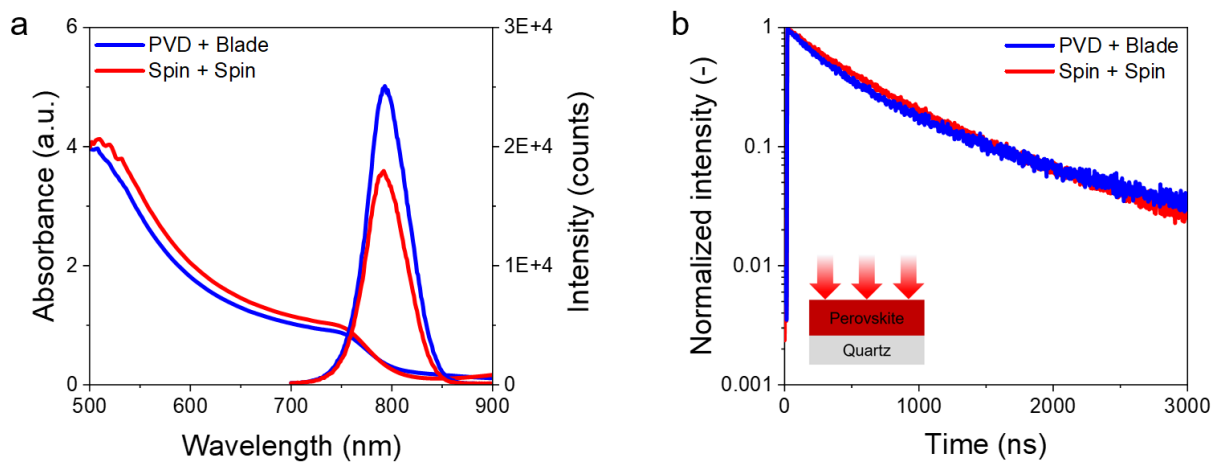


Figure S9: Optoelectronic properties of perovskite films fabricated by the PVD/blade process (PVD + Blade) and by two-step spin coating (Spin + Spin) on quartz. a) Ultraviolet-visible (UV-Vis) absorbance and photoluminescence (PL) spectra, b) time-resolved photoluminescence (TRPL) decays. The decay lifetimes are obtained by fitting the measurement with the bi-exponential decay function $I(t) = A_1 \exp\left(-\frac{t}{\tau_1}\right) + A_2 \exp\left(-\frac{t}{\tau_2}\right)$. The fitting parameters are provided in Table S1.

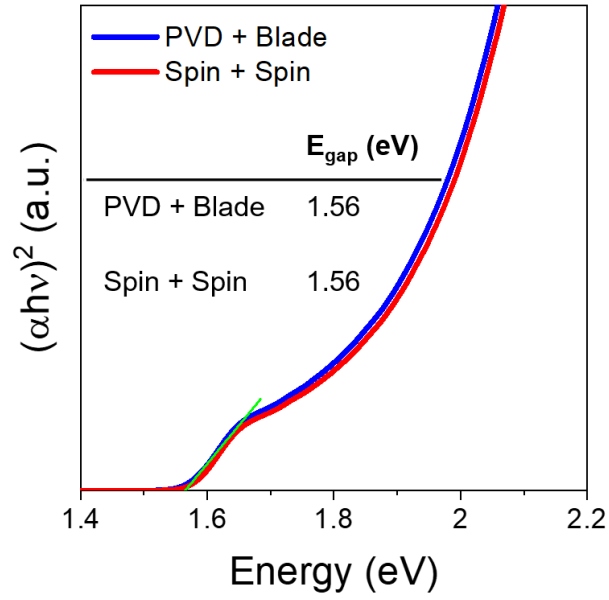


Figure S10: Tauc plot as a function of $(\alpha h\nu)^2$ versus energy of the perovskite films by the PVD/blade process (PVD + Blade) and by two-step spin coating (Spin + Spin) on quartz. The extracted bandgap energy is 1.56 eV for both methods.

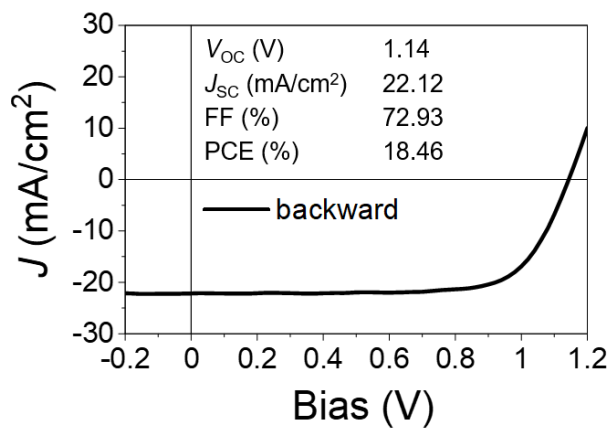


Figure S11: Photovoltaic performance of PSC with two-step spin coated perovskite absorber layer (Spin + Spin) and blade coated charge transporting layers.

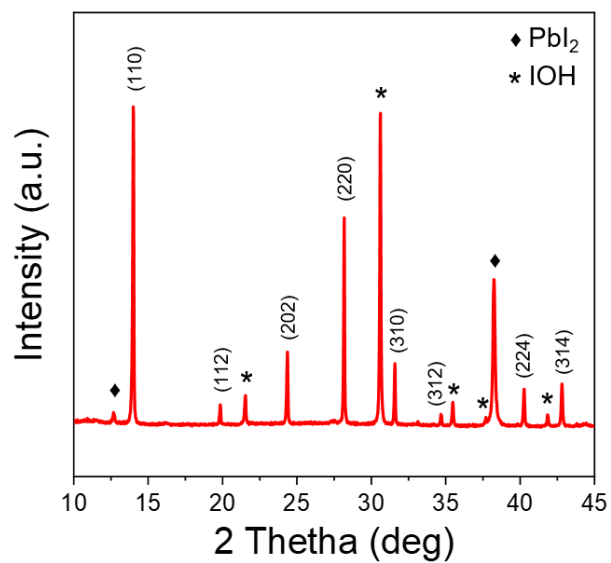


Figure S12: XRD pattern of PSC device. Perovskite crystal planes are indexed. PbI₂ is labeled by ◆ and IOH by *.

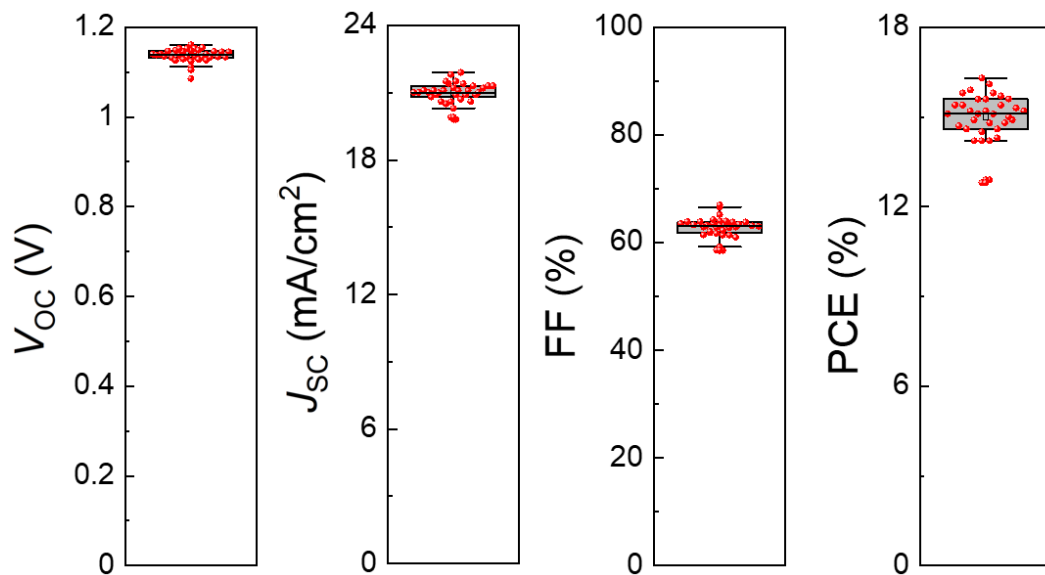


Figure S13: Photovoltaic performance overview of 36 PSC devices on 5 cm x 5 cm sample with blade coated charge transporting layers and perovskite fabricated by PVD/blade process.

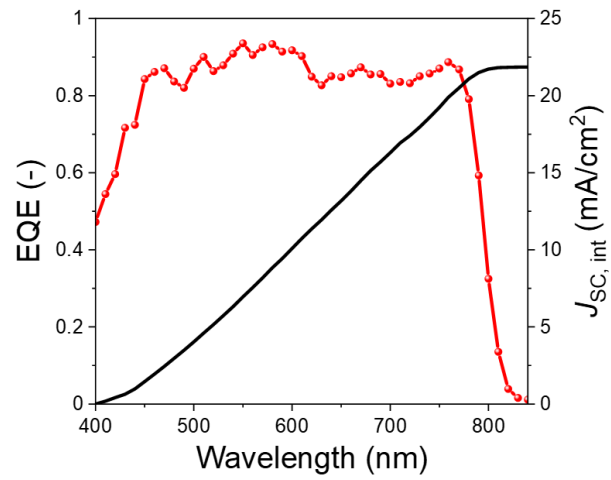


Figure S14: EQE spectrum with integrated J_{SC} value of 21.86 mA/cm² for the PSC device.

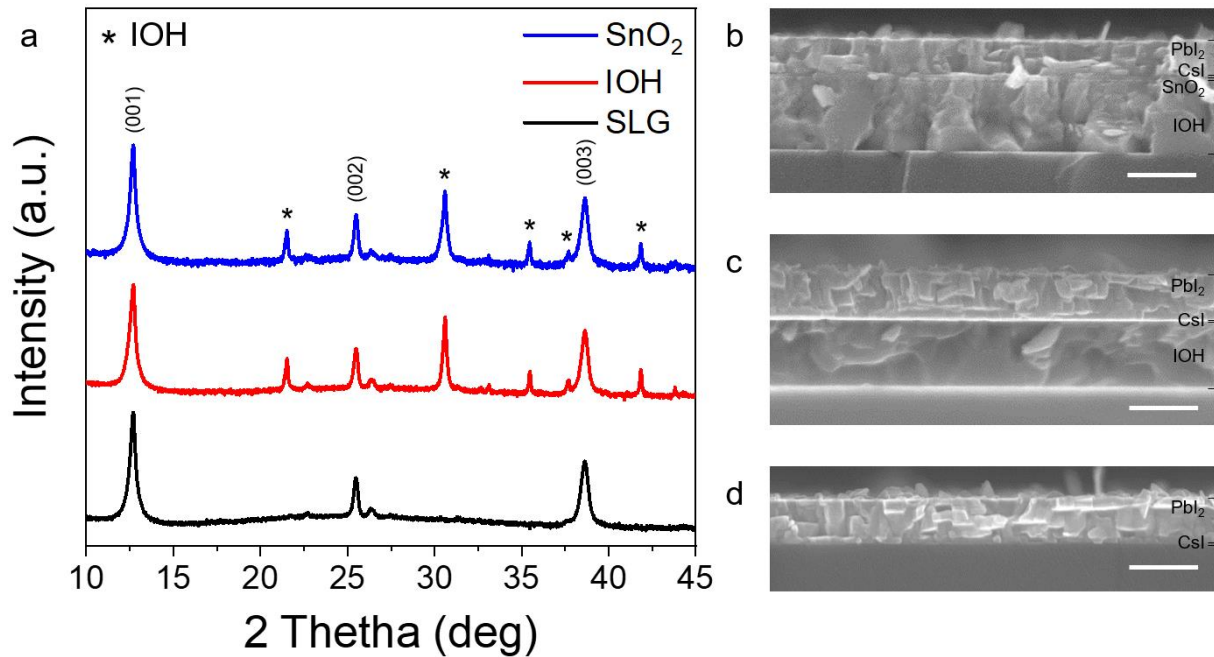


Figure S15: XRD patterns of the inorganic halide template (PbI₂/CsI), sequentially evaporated on SnO₂ (blue), on IOH (red) and on soda-lime glass (SLG, black). a) PbI₂ crystal planes are indexed and IOH is labeled by *. Corresponding SEM cross-section view images of the inorganic halide template on b) SnO₂, c) IOH and d) SLG. The scale bar is 500 nm.

Table S1: Fitting parameters of the bi-exponential decay function of the time-resolved photoluminescence (TRPL) measurement of the perovskite films obtained by PVD/blade process and by two-step spin coating. Average decay time τ was calculated according to: $\tau = \frac{A_1\tau_1 + A_2\tau_2}{A_1 + A_2}$.

Method	A_1	τ_1 (ns)	A_2	τ_2 (ns)	τ (ns)
PVD + Blade	2094.29	342.52	737.74	1405.7	619.48
Spin + Spin	3107.67	395.59	1603.44	1148.4	651.81

Table S2: Summary of the chart in Figure 4d with selected work of perovskite solar cells with indicated layers fabricated by scalable deposition methods.

YEAR	SCALABLE LAYERS	PCE	STACK	REF
2019	PVK	20.2	FTO/SnO ₂ /PVK/Spiro-OMeTAD/Ag	1
2020	PVK	19.6	FTO/SnO ₂ /PVK/Spiro-OMeTAD/Au	2
2020	PVK	20.3	ITO/SnO ₂ /PCBM/PVK/Spiro-OMeTAD/Au	3
2021	PVK	20.6	ITO/MeO-2PACz/PVK/PCBM/BCP/Ag	4
2016	PVK/ETL	18.3	FTO/c-TiO ₂ /PVKPTAA/Au	5
2016	PVK/ETL	15.6	FTO/c-TiO ₂ /m-TiO ₂ /PVK/Spiro-OMeTAD/Au	6
2017	PVK/ETL	20.1	FTO/TiO ₂ /PVK/PTAA/Ag	7
2017	PVK/ETL	16.6	FTO/c-TiO ₂ /PVK/Spiro-OMeTAD/Au	8
2017	PVK/ETL	18.6	FTO/c-TiO ₂ /m-TiO ₂ /PVK/Spiro-OMeTAD/Au	1
2017	PVK/ETL	15.8	FTO/C60/PVK/Spiro-OMeTAD/Ag	9
2018	PVK/ETL	17.3	FTO/SnO ₂ /PVK/Spiro-OMeTAD/Au	10
2018	PVK/ETL	18.7	ITO/TiO ₂ /PVK/Spiro-OMeTAD/Au	11
2020	PVK/ETL	20.6	ITO/MeO-2PACz/PVK/C60/BCP/Cu	12
2015	PVK/ETL/HTL	13.3	FTO/c-TiO ₂ /m-TiO ₂ /PVK/P3HT/Au	13
2017	PVK/ETL/HTL	14.0	FTO/c-TiO ₂ /m-TiO ₂ /m-ZrO ₂ /PVK/Carbon	14
2018	PVK/ETL/HTL	20.3	ITO/PTAA/PVK/C60/BCP/Cu	15
2018	PVK/ETL/HTL	19.4	FTO/c-TiO ₂ /PVK/Spiro-OMeTAD/Au	16
2018	PVK/ETL/HTL	16.8	FTO/c-TiO ₂ /PVK/Spiro-OMeTAD/Au	17
2020	PVK/ETL/HTL	17.8	ITO/SnO ₂ /SAM/PVK/PDCBT/Ta-WO _x /Ag	18
2020	PVK/ETL/HTL	21.7	FTO/TiO ₂ /PVK/PCBM/Ag	19
2020	PVK/ETL/HTL	16.3	ITO/SnO ₂ /PVK/Spiro-OMeTAD/Au	20
2021	PVK/ETL/HTL	23.6	ITO/PTAA/PVK/C60/BCP/Cu	21

2021	PVK/ETL/HTL	18.9	FTO/TiO ₂ /PVK/MoO ₃ /NPB/Au	22
2021	PVK/ETL/HTL	23.2	ITO/PTAA/PVK/C60/BCP/Cu	23
2021	PVK/ETL/HTL	18.7	IOH/SnO ₂ /PVK/Spiro-OMeTAD/Au	This work
2021	PVK/ETL/HTL	15.9	FTO/c-TiO ₂ /mp-TiO ₂ /PVK/Spiro-OMeTAD/Ag	24
2021	PVK/ETL/HTL	19.4	ITO/SnO ₂ /PVK/HTL/Ta-WO _x /Au	25
2021	PVK/ETL/HTL	16.1	TCO/CuPc/PVK/C60/BCP/Ag	26

REFERENCES of Table S2

- (1) Yang, M.; Li, Z.; Reese, M. O.; Reid, O. G.; Kim, D. H.; Siol, S.; Klein, T. R.; Yan, Y.; Berry, J. J.; Van Hest, M. F. A. M.; Zhu, K. Perovskite Ink with Wide Processing Window for Scalable High-Efficiency Solar Cells. *Nat. Energy* **2017**, *2* (5), 1–9. <https://doi.org/10.1038/nenergy.2017.38>.
- (2) Lim, K. S.; Lee, D. K.; Lee, J. W.; Park, N. G. 17% Efficient Perovskite Solar Mini-Module: Via Hexamethylphosphoramide (HMPA)-Adduct-Based Large-Area D-Bar Coating. *J. Mater. Chem. A* **2020**, *8* (18), 9345–9354. <https://doi.org/10.1039/d0ta02017f>.
- (3) Li, J.; Wang, H.; Chin, X. Y.; Dewi, H. A.; Vergeer, K.; Goh, T. W.; Lim, J. W. M.; Lew, J. H.; Loh, K. P.; Soci, C.; Sum, T. C.; Bolink, H. J.; Mathews, N.; Mhaisalkar, S.; Bruno, A. Highly Efficient Thermally Co-Evaporated Perovskite Solar Cells and Mini-Modules. *Joule* **2020**, *4* (5), 1035–1053. <https://doi.org/10.1016/j.joule.2020.03.005>.
- (4) Li, J.; Dewi, H. A.; Wang, H.; Zhao, J.; Tiwari, N.; Yantara, N.; Malinauskas, T.; Getautis, V.; Savenije, T. J.; Mathews, N.; Mhaisalkar, S.; Bruno, A. Co-Evaporated MAPbI₃ with Graded Fermi Levels Enables Highly Performing, Scalable, and Flexible p-i-n Perovskite Solar Cells. *Adv. Funct. Mater.* **2021**, *2103252*, 1–11. <https://doi.org/10.1002/adfm.202103252>.
- (5) Heo, J. H.; Lee, M. H.; Jang, M. H.; Im, S. H. Highly Efficient CH₃NH₃PbI₃-xCl_x Mixed Halide Perovskite Solar Cells Prepared by Re-Dissolution and Crystal Grain Growth via Spray Coating. *J. Mater. Chem. A* **2016**, *4* (45), 17636–17642. <https://doi.org/10.1039/c6ta06718b>.
- (6) Leyden, M. R.; Jiang, Y.; Qi, Y. Chemical Vapor Deposition Grown Formamidinium Perovskite Solar Modules with High Steady State Power and Thermal Stability. *J. Mater. Chem. A* **2016**, *4* (34), 13125–13132. <https://doi.org/10.1039/c6ta04267h>.
- (7) He, M.; Li, B.; Cui, X.; Jiang, B.; He, Y.; Chen, Y.; O'Neil, D.; Szymanski, P.; Ei-Sayed, M. A.; Huang, J.; Lin, Z. Meniscus-Assisted Solution Printing of Large-Grained Perovskite Films for High-Efficiency Solar Cells. *Nat. Commun.* **2017**, *8* (May). <https://doi.org/10.1038/ncomms16045>.
- (8) Jiang, Y.; Leyden, M. R.; Qiu, L.; Wang, S.; Ono, L. K.; Wu, Z.; Juarez-Perez, E. J.; Qi, Y. Combination of Hybrid CVD and Cation Exchange for Upscaling Cs-Substituted Mixed Cation Perovskite Solar Cells with High Efficiency and Stability. *Adv. Funct. Mater.* **2018**, *28* (1). <https://doi.org/10.1002/adfm.201703835>.
- (9) Borchert, J.; Milot, R. L.; Patel, J. B.; Davies, C. L.; Wright, A. D.; Martínez Maestro, L.; Snaith, H. J.; Herz, L. M.; Johnston, M. B. Large-Area, Highly Uniform Evaporated Formamidinium Lead Triiodide Thin Films for Solar Cells. *ACS Energy Lett.* **2017**, *2* (12), 2799–2804.

- <https://doi.org/10.1021/acscenergylett.7b00967>.
- (10) Luo, L.; Zhang, Y.; Chai, N.; Deng, X.; Zhong, J.; Huang, F.; Peng, Y.; Ku, Z.; Cheng, Y. B. Large-Area Perovskite Solar Cells with CsxFA1-xPbI3-yBry Thin Films Deposited by a Vapor-Solid Reaction Method. *J. Mater. Chem. A* **2018**, *6* (42), 21143–21148. <https://doi.org/10.1039/c8ta06557h>.
 - (11) Li, J.; Munir, R.; Fan, Y.; Niu, T.; Liu, Y.; Zhong, Y.; Yang, Z.; Tian, Y.; Liu, B.; Sun, J.; Smilgies, D. M.; Thoroddsen, S.; Amassian, A.; Zhao, K.; Liu, S. (Frank). Phase Transition Control for High-Performance Blade-Coated Perovskite Solar Cells. *Joule* **2018**, *2* (7), 1313–1330. <https://doi.org/10.1016/j.joule.2018.04.011>.
 - (12) Roß, M.; Gil-Escrig, L.; Al-Ashouri, A.; Tockhorn, P.; Jošt, M.; Rech, B.; Albrecht, S. Co-Evaporated p-i-n Perovskite Solar Cells beyond 20% Efficiency: Impact of Substrate Temperature and Hole-Transport Layer. *ACS Appl. Mater. Interfaces* **2020**, *12* (35), 39261–39272. <https://doi.org/10.1021/acscami.0c10898>.
 - (13) Razza, S.; Di Giacomo, F.; Matteocci, F.; Cinà, L.; Palma, A. L.; Casaluci, S.; Cameron, P.; D'Epifanio, A.; Licoccia, S.; Reale, A.; Brown, T. M.; Di Carlo, A. Perovskite Solar Cells and Large Area Modules (100 Cm²) Based on an Air Flow-Assisted PbI₂ Blade Coating Deposition Process. *J. Power Sources* **2015**, *277*, 286–291. <https://doi.org/10.1016/j.jpowsour.2014.12.008>.
 - (14) Hu, Y.; Si, S.; Mei, A.; Rong, Y.; Liu, H.; Li, X.; Han, H. Stable Large-Area (10 × 10 Cm²) Printable Mesoscopic Perovskite Module Exceeding 10% Efficiency. *Sol. RRL* **2017**, *1* (2), 2–7. <https://doi.org/10.1002/solr.201600019>.
 - (15) Deng, Y.; Zheng, X.; Bai, Y.; Wang, Q.; Zhao, J.; Huang, J. Surfactant-Controlled Ink Drying Enables High-Speed Deposition of Perovskite Films for Efficient Photovoltaic Modules. *Nat. Energy* **2018**, *3* (7), 560–566. <https://doi.org/10.1038/s41560-018-0153-9>.
 - (16) Yang, M.; Kim, D. H.; Klein, T. R.; Li, Z.; Reese, M. O.; Tremolet De Villers, B. J.; Berry, J. J.; Van Hest, M. F. A. M.; Zhu, K. Highly Efficient Perovskite Solar Modules by Scalable Fabrication and Interconnection Optimization. *ACS Energy Lett.* **2018**, *3* (2), 322–328. <https://doi.org/10.1021/acscenergylett.7b01221>.
 - (17) Di Giacomo, F.; Shanmugam, S.; Fledderus, H.; Bruijnaers, B. J.; Verhees, W. J. H.; Dorenkamper, M. S.; Veenstra, S. C.; Qiu, W.; Gehlhaar, R.; Merckx, T.; Aernouts, T.; Andriessen, R.; Galagan, Y. Up-Scalable Sheet-to-Sheet Production of High Efficiency Perovskite Module and Solar Cells on 6-in. Substrate Using Slot Die Coating. *Sol. Energy Mater. Sol. Cells* **2018**, *181* (August 2017), 53–59. <https://doi.org/10.1016/j.solmat.2017.11.010>.
 - (18) Yang, F.; Dong, L.; Jang, D.; Tam, K. C.; Zhang, K.; Li, N.; Guo, F.; Li, C.; Arrive, C.; Bertrand, M.; Brabec, C. J.; Egelhaaf, H. J. Fully Solution Processed Pure α -Phase Formamidinium Lead Iodide Perovskite Solar Cells for Scalable Production in Ambient Condition. *Adv. Energy Mater.* **2020**, *10* (42), 1–11. <https://doi.org/10.1002/aenm.202001869>.
 - (19) Du, M.; Zhu, X.; Wang, L.; Wang, H.; Feng, J.; Jiang, X.; Cao, Y.; Sun, Y.; Duan, L.; Jiao, Y.; Wang, K.; Ren, X.; Yan, Z.; Pang, S.; Liu, S. High-Pressure Nitrogen-Extraction and Effective Passivation to Attain Highest Large-Area Perovskite Solar Module Efficiency. *Adv. Mater.* **2020**, *32* (47), 1–10. <https://doi.org/10.1002/adma.202004979>.
 - (20) Bishop, J. E.; Read, C. D.; Smith, J. A.; Routledge, T. J.; Lidzey, D. G. Fully Spray-Coated Triple-Cation Perovskite Solar Cells. *Sci. Rep.* **2020**, *10* (1), 1–8. <https://doi.org/10.1038/s41598-020-63674-5>.
 - (21) Chen, S.; Dai, X.; Xu, S.; Jiao, H.; Zhao, L.; Huang, J. Stabilizing Perovskite-Substrate Interfaces for High-Performance Perovskite Modules. *Science (80-.)*. **2021**, *373* (6557), 902 LP – 907. <https://doi.org/10.1126/science.abi6323>.
 - (22) Feng, J.; Jiao, Y.; Wang, H.; Zhu, X.; Sun, Y.; Du, M.; Cao, Y.; Yang, D.; Liu, S. (Frank). High-Throughput Large-Area Vacuum Deposition for High-Performance Formamidinium-Based Perovskite Solar Cells.

- Energy Environ. Sci.* **2021**, *14* (5), 3035–3043. <https://doi.org/10.1039/d1ee00634g>.
- (23) Chen, S.; Xiao, X.; Gu, H.; Huang, J. Iodine Reduction for Reproducible and High-Performance Perovskite Solar Cells and Modules. **2021**, 1–7. <https://doi.org/10.1126/sciadv.abe8130>.
- (24) Adugna, G. B.; Abate, S. Y.; Wu, W. T.; Tao, Y. T. Toward Large-Area and Fully Solution-Sheared Perovskite Solar Cells. *ACS Appl. Mater. Interfaces* **2021**. <https://doi.org/10.1021/acsami.1c03460>.
- (25) Yang, F.; Dong, L.; Jang, D.; Saparov, B.; Tam, K. C.; Zhang, K.; Li, N.; Brabec, C. J.; Egelhaaf, H. J. Low Temperature Processed Fully Printed Efficient Planar Structure Carbon Electrode Perovskite Solar Cells and Modules. *Adv. Energy Mater.* **2021**, *2101219*. <https://doi.org/10.1002/aenm.202101219>.
- (26) Seto, S. Inverted Planer Perovskite Solar Cells Fabricated by All Vapor Phase Process. *Jpn. J. Appl. Phys.* **2021**, *60*, 0–6. <https://doi.org/10.35848/1347-4065/abdad3>.

REFERENCES

- (1) Fu, F.; Kranz, L.; Yoon, S.; Löckinger, J.; Jäger, T.; Perrenoud, J.; Feurer, T.; Gretener, C.; Buecheler, S.; Tiwari, A. N. Controlled Growth of PbI₂ Nanoplates for Rapid Preparation of CH₃NH₃PbI₃ in Planar Perovskite Solar Cells. *Phys. Status Solidi Appl. Mater. Sci.* **2015**, *212* (12), 2708–2717. <https://doi.org/10.1002/pssa.201532442>.
- (2) Jiang, Y.; Feurer, T.; Carron, R.; Sevilla, G. T.; Moser, T.; Pisoni, S.; Erni, R.; Rossell, M. D.; Ochoa, M.; Hertwig, R.; Tiwari, A. N.; Fu, F. High-Mobility In₂O₃:H Electrodes for Four-Terminal Perovskite/CuInSe₂Tandem Solar Cells. *ACS Nano* **2020**, *14* (6), 7502–7512. <https://doi.org/10.1021/acsnano.0c03265>.
- (3) Song, Z.; Wathage, S. C.; Phillips, A. B.; Tompkins, B. L.; Ellingson, R. J.; Heben, M. J. Impact of Processing Temperature and Composition on the Formation of Methylammonium Lead Iodide Perovskites. *Chem. Mater.* **2015**, *27* (13), 4612–4619. <https://doi.org/10.1021/acs.chemmater.5b01017>.
- (4) Kwon, U.; Hasan, M. M.; Yin, W.; Kim, D.; Ha, N. Y.; Lee, S.; Ahn, T. K.; Park, H. J. Investigation into the Advantages of Pure Perovskite Film without PbI₂ for High Performance Solar Cell. *Sci. Rep.* **2016**, *6*, 1–9. <https://doi.org/10.1038/srep35994>.
- (5) Jiang, Q.; Zhao, Y.; Zhang, X.; Yang, X.; Chen, Y.; Chu, Z.; Ye, Q.; Li, X.; Yin, Z.; You, J. Surface Passivation of Perovskite Film for Efficient Solar Cells. *Nat. Photonics* **2019**, *13* (7), 460–466. <https://doi.org/10.1038/s41566-019-0398-2>.
- (6) Liu, K.; Liang, Q.; Qin, M.; Shen, D.; Yin, H.; Ren, Z.; Zhang, Y.; Zhang, H.; Fong, P. W. K.; Wu, Z.; Huang, J.; Hao, J.; Zheng, Z.; So, S. K.; Lee, C. S.; Lu, X.; Li, G. Zwitterionic-

Surfactant-Assisted Room-Temperature Coating of Efficient Perovskite Solar Cells. *Joule* **2020**, *4* (11), 2404–2425. <https://doi.org/10.1016/j.joule.2020.09.011>.